Slip velocity of rigid fibers in turbulent channel flow

L. Zhao, C. Marchioli, and H. I. Andersson

Citation: Physics of Fluids (1994-present) **26**, 063302 (2014); doi: 10.1063/1.4881942
View online: http://dx.doi.org/10.1063/1.4881942
View Table of Contents: http://scitation.aip.org/content/aip/journal/pof2/26/6?ver=pdfcov
Published by the AIP Publishing

PHYSICS OF FLUIDS **26**, 063302 (2014)

Slip velocity of rigid fibers in turbulent channel flow

L. Zhao,[1] C. Marchioli,[2,3] and H. I. Andersson[1]
[1]*Department of Energy and Process Engineering, Norwegian University of Science and Technology, 7491 Trondheim, Norway*
[2]*Department of Electrical, Management and Mechanical Engineering, University of Udine, 33100 Udine, Italy*
[3]*Department of Fluid Mechanics, CISM International Centre for Mechanical Sciences, 33100 Udine, Italy*

(Received 15 November 2013; accepted 27 May 2014; published online 20 June 2014)

In this study, the slip velocity between rigid fibers and a viscous carrier fluid is investigated for the reference case of turbulent channel flow. The statistical moments of the slip velocity are evaluated modelling fibers as prolate spheroids with Stokes number, *St*, ranging from 1 to 100 and aspect ratio, λ, ranging from 3 to 50. Statistics are compared one-to-one with those obtained for spherical particles ($\lambda = 1$) to highlight effects due to fiber elongation. Comparison is also made at different Reynolds numbers (Re_τ =150, 180, and 300 based on the fluid shear velocity) to discuss effects due to an increase of turbulent fluctuations. Results show that elongation has a quantitative effect on slip velocity statistics, particularly evident for fibers with small *St*. As *St* increases, differences due to the aspect ratio tend to vanish and the relative translational motion between individual fibers and surrounding fluid is controlled by fiber inertia through preferential concentration. A clear manifestation of inertial effects is the different distribution of slip velocities for fibers trapped in sweep/ejection events and for fibers segregated in near-wall fluid streaks. The corresponding conditional probability distribution functions, shown here for the streamwise and wall-normal slip velocity components, are found to be non-Gaussian, thus suggesting that fiber motion relative to the fluid in high-shear flow regions may not be modelled as a pure diffusion process with constant diffusion coefficient. For the range of simulation parameters investigated, no significant Reynolds number effects are observed, indicating that fiber dynamics exhibit a scaling behavior with respect to the shear velocity up to Re_τ =300. © *2014 AIP Publishing LLC*. [http://dx.doi.org/10.1063/1.4881942]

I. INTRODUCTION

Suspensions of solid non-spherical particles in turbulent flow are commonly found in industry and nature. Pulp and paper making,[1] food processing,[2] and dispersion of pollen[3] and soot particles[4] in the environment are just few of the countless examples that could be mentioned. Because of the practical importance of such suspensions, knowledge of non-spherical particle behavior in a turbulent environment is deemed crucial not only for the design and optimization of operation units in industrial applications, but also for the physical understanding of natural processes. This knowledge, however, is still limited, especially the two-way and four-way coupling effects, as discussed in Zhao and van Wachem.[5] The reason has to do with the complex interaction between particles with non-spherical shape and the surrounding fluid, equally influenced by particle translation and rotation. The reader is referred to the Special Issue on anisotropic particles in turbulence published recently in Acta Mechanica for a comprehensive collection of current research achievements and survey of open issues in the field.[6]

In this paper, we examine the role of particle shape on particle-turbulence interaction focusing on one essential Lagrangian observable: the slip velocity vector, defined as $\Delta\mathbf{u} = \mathbf{u}_f - \mathbf{u}_p$, where $\mathbf{u}_f$ is the fluid velocity seen by the particle along its trajectory and $\mathbf{u}_p$ is the particle translational velocity. In classical Lagrangian Stochastic approaches, however, $\mathbf{u}_f$ and $\mathbf{u}_p$ are handled as two

separate variables. To perform our analysis, we consider a turbulent suspension of rigid fibers, a specific type of elongated non-spherical particles that occurs over a wide range of length scales. The slip velocity is chosen here in view of its paramount importance in many practical situations, which are briefly outlined in the following. In one-way coupling simulations, it is the only flow variable that determines the drag force experienced by the particles. In two-way coupled simulations, the slip velocity is crucial for the modulation of turbulence since it determines the reaction force exerted by the particles on the fluid.[5,7] In CFD (Computational Fluid Dynamics) calculations, algebraic models for the slip velocity are often used to simulate gas-liquid flows based on correlations that couple the particle force balance equation with the carrier fluid momentum equation.[8–10] To prescribe an algebraic relation for $\Delta\mathbf{u}$, however, these models typically assume that a local equilibrium between the phases may be reached over short spatial distances and compute the slip velocity based on the acceleration of the particle generated by gravity (and/or a centrifugal force) and on a diffusion term accounting for turbulent dispersion due to the action of fluid eddies. The validity of such equilibrium assumptions and hence the reliability of existing algebraic slip models appear limited, but could be improved if new slip velocity datasets taken from DNS-based computer experiments are made available for validation purposes. Such datasets could also be used for developing sub-grid scale closures for particle motion in large-eddy simulations of turbulence, where filtering effects on the slip velocity represent a key modeling variable.[11,12] The slip velocity is furthermore at the heart of the so-called crossing trajectory effect.[13,14] Under the influence of an external force field or its own inertia, a particle deviates from the trajectories of its surrounding fluid parcels. Inertial particles therefore lose velocity correlation more rapidly than the neighbouring fluid and disperse less.[15] The decorrelation of the fluid velocity fluctuations along the discrete particle paths can be accounted for by a modified integral time scale.[14] Simonin *et al.*[16] further discussed Csanady's[14] modelling of the crossing-trajectory effect, whereas a particularly thorough discussion was provided by Minier and Peirano.[17] Oesterlé[18] recently analyzed the crossing trajectory phenomenon in a homogeneous shear flow by means of a Langevin-type stochastic model.

In a recent paper,[19] we examined the slip velocity of small spherical particles with different inertia, aiming to explore their dynamics in wall-bounded turbulence and to provide statistical information for possible inclusion in models. Slip velocity statistics were computed for the reference case of turbulent channel flow at shear Reynolds number $Re_\tau = 150$ based on the channel half height, considering a dilute suspension of particles with Stokes number (the ratio between the particle response time and the viscous time scale of the flow) in the range $1 \leq St \leq 100$. Results showed a monotonic increase of the slip velocity fluctuations for increasing particle inertia, with standard deviations significantly larger than the corresponding mean value. In this paper, we build on those results and study the slip velocity of elongated rigid fibers, thus including the effect of fiber aspect ratio, λ, on $\Delta\mathbf{u}$. To these aims, statistics were extracted from a comprehensive repository of DNS data obtained in the (Re_τ, St, λ) parameter space and computed considering conditional averaging rather than averaging over discrete Eulerian grid points. These statistics, along with corresponding raw data, are made freely available to interested users and can be used as reference test case for code benchmarking and/or model development and validation. It should be noted that, although closely related, the present choice of handling directly the slip velocity is different from the choice made in classical Lagrangian formulations for flows laden with spherical particles, e.g., Minier and Peirano.[17]

To the best of our knowledge, there are very few papers in the archival literature[5,20] in which slip velocity statistics for fibers in channel flow have been presented. Mortensen *et al.*[20] performed one-way coupled simulation of turbulent channel flow at $Re_\tau = 180$ and focused on the mean streamwise slip velocity Δu for fiber-like prolate spheroids with aspect ratio λ equal to 1, 3, and 10 and Stokes number $St = 5$ and 30. It was found that Δu is (i) negative near the wall, where fibers move faster than the local fluid due to segregation into low-speed streaks, and (ii) positive in the center of the channel, where fibers lag the fluid as a consequence of their interaction with large-scale (rather than small-scale) flow structures. Elongation was observed to increase monotonically the magnitude of the streamwise slip velocity near the wall. Zhao and van Wachem[5] also discussed mean slip velocity profiles but for spheroids with $\lambda = 3$ and $St = 5$ at $Re_\tau = 150$: Therefore, no indication of elongation, inertia, and turbulence intensity effects on $\Delta\mathbf{u}$ could be provided. Also, Zhao and

van Wachem[5] considered full four-way coupling by including a feedback of the particles on the fluid together with the effect of particle-particle collisions. These effects, however, turned out to be rather weak at the same volume fraction as that considered in our study. In practice, as will be discussed in Sec. IV, only minor quantitative modifications were observed with respect to the uncoupled simulations. Considering the purpose of the present paper (statistical characterization of aspect ratio effects on the slip velocity at varying fiber inertia in wall-bounded turbulence) we decided to keep the simplest simulation setting and hence stick to the dilute flow condition.

II. MATHEMATICAL MODELING AND GOVERNING EQUATIONS

We simulate the motion of rigid fibers in turbulent channel flow using an Eulerian-Lagrangian approach. In this section, the Eulerian formulation of the fluid phase is first provided, followed by the Lagrangian representation of the fibers.

A. Eulerian fluid representation

In this work, the carrier fluid is Newtonian (with dynamic viscosity μ) and incompressible (with density ρ). The fluid motion is governed by the following mass and momentum conservation equations non-dimensionalized by the channel half-height h and the kinematic viscosity of the fluid ν:

$$\nabla \cdot \mathbf{u} = 0; \qquad \frac{\partial \mathbf{u}}{\partial t} + (\mathbf{u} \cdot \nabla)\mathbf{u} = -\nabla p + \frac{1}{Re_\tau}\nabla^2 \mathbf{u}, \tag{1}$$

where $\mathbf{u}$ and p denote the fluid velocity vector and the pressure, respectively. Here, the wall-friction velocity $u_\tau = \sqrt{\tau_{wall}/\rho}$, where τ_{wall} is the wall shear stress. The frictional Reynolds number is $Re_\tau = hu_\tau/\nu$. Pressure is normalized by ρu_τ^2.

The flow is driven by a constant mean pressure gradient along the positive streamwise (x) direction, and is unaffected by the presence of the fibers, i.e., there is no reaction force from the fibers in the fluid momentum Eq. (1). The present study is therefore one-way coupled and applies only to dilute fiber suspensions. One-way coupling allows to investigate slip velocity statistics by letting different-inertia fibers evolve in exactly the same instantaneous flow field.

B. Lagrangian representation of fiber

The fibers are modelled as point-wise prolate rigid, and elastically rebounding spheroids with aspect ratio $\lambda = b/a$ where b and a are the semi-major and semi-minor axes, respectively. The mathematical modeling stems from the methodology outlined by Zhang *et al.*[21] and subsequently adopted by Mortensen *et al.*[20] and by Marchioli *et al.*[22] The translational and rotational motion of a single fiber of mass m is governed by the following equations:

$$m\frac{\mathrm{d}\mathbf{u}_p}{\mathrm{d}t} = \mathbf{F}, \tag{2}$$

$$\frac{\mathrm{d}(\mathbf{I}'\cdot\boldsymbol{\omega}')}{\mathrm{d}t} + \boldsymbol{\omega}' \times (\mathbf{I}'\cdot\boldsymbol{\omega}') = \mathbf{N}' \tag{3}$$

written with respect to two different Cartesian frames of reference: Eq. (2) is formulated in the *inertial frame* $\boldsymbol{x} = \langle x, y, z\rangle$ with x, y, and z the streamwise, spanwise, and wall-normal flow directions, respectively. Equation (3) is formulated in the *fiber frame* $\boldsymbol{x}' = \langle x', y', z'\rangle$ with origin at the particle center of mass and coordinate axes aligned with the principal directions of inertia. Therefore, $\mathbf{u}_p = \mathrm{d}\mathbf{x}_p/\mathrm{d}t$ denotes the translational fiber velocity vector in the inertial frame; whereas $\mathbf{I}'$, $\boldsymbol{\omega}'$, and $\mathbf{N}'$ represent the moment of inertia tensor, the angular velocity of the fiber and the torque in the fiber frame, respectively. If the fibers are small enough to assume that the surrounding flow can be considered as Stokesian, the drag force $\mathbf{F}$ can be expressed as

$$\mathbf{F} = \mu\mathbf{A}^t\mathbf{K}'\mathbf{A}\cdot(\mathbf{u}_f - \mathbf{u}_p) = \mu\mathbf{A}^t\mathbf{K}'\mathbf{A}\cdot\Delta\mathbf{u}, \tag{4}$$

where the fluid velocity at the fiber position $\mathbf{u}_f$ is obtained using a 6th-order Lagrangian polynomial interpolation scheme and $\mathbf{K}'$ is the resistance tensor in the fiber frame. Here, $\mathbf{A}$ denotes the orthogonal transformation matrix which relates the same vector in the two different frames through the linear transformation $\mathbf{x} = \mathbf{A}\,\mathbf{x}'$. For a prolate spheroid with z' along the major axis, the off-diagonal elements of $\mathbf{K}'$ are identically zero and the diagonal elements become:[5,21,23]

$$\begin{aligned} k'_{xx} &= k'_{yy} = \frac{16\pi a(\lambda^2-1)^{3/2}}{(2\lambda^2-3)\ln(\lambda+(\lambda^2-1)^{1/2})+\lambda(\lambda^2-1)^{1/2}} \\ k'_{zz} &= \frac{8\pi a(\lambda^2-1)^{3/2}}{(2\lambda^2-1)\ln(\lambda+(\lambda^2-1)^{1/2})-\lambda(\lambda^2-1)^{1/2}}. \end{aligned} \tag{5}$$

Note that the corresponding expressions in the earlier papers by Mortensen *et al.*[20] and Marchioli *et al.*[22] suffer from some unfortunate typos. The expression for the hydrodynamic drag force for a particle with arbitrary shape was derived by Brenner[24] assuming creep flow conditions, i.e., small fiber Reynolds number, $Re_p = 2a|\Delta\mathbf{u}|/\nu$. In agreement with the definition adopted for the fiber response time, the fiber Reynolds number Re_p is somewhat arbitrarily based on the semi-minor axis a. Alternative definitions could involve the semi-major axis b or the diameter of the volume-equivalent sphere. In our simulations, Re_p based on the mean streamwise slip velocity is always significantly smaller than unity with the exception of the $St = 100$ particles, for which maximum values slightly above 1 are obtained well inside the buffer region. In this case underestimation of the drag force would amount to roughly 15% of the Stokes drag for the spherical particles, according to the correction of Schiller and Naumann.[25] It should be mentioned, however, that an *effective* particle Reynolds number might be higher than Re_p based on the mean slip velocity, partly because 2a is the shortest geometrical length scale of a prolate ellipsoid and partly because the instantaneous slip velocity may exceed the mean slip velocity, as pointed out by Zhao *et al.*[19] for spherical particles. Note that Schiller-Naumann-like corrections for non-spherical particles are currently unavailable (see also discussion in Sec. III). To focus on effects of fiber shape and inertia, gravity (which is known to influence the slip velocity by decorrelating particle velocity from the fluid velocity seen) and lift forces were ignored in the present study.

The torque components N'_i can be expressed as follows:

$$\begin{aligned} N'_x &= \tfrac{16\pi\mu a^3\lambda}{3(\beta_0+\lambda^2\gamma_0)}[(1-\lambda^2)S'_{yz}+(1+\lambda^2)(\Omega'_x-\omega'_x)] \\ N'_y &= \tfrac{16\pi\mu a^3\lambda}{3(\alpha_0+\lambda^2\gamma_0)}[(\lambda^2-1)S'_{xz}+(1+\lambda^2)(\Omega'_y-\omega'_y)] \\ N'_z &= \tfrac{32\pi\mu a^3\lambda}{3(\alpha_0+\beta_0)}(\Omega'_z-\omega'_z). \end{aligned} \tag{6}$$

The parameters α_0, β_0, and γ_0 depend on the aspect ratio λ, and their expressions were first derived by Jeffery[26] for an ellipsoidal particle in creeping motion. Here, S'_{ij} and Ω'_i denote elements of the fluid rate-of-strain tensor and rate-of-rotation vector, respectively. The vorticity of the fluid flow field is thus $2\Omega'_i$.

The shape of the fiber is characterized by the aspect ratio λ, whereas its ability to interact with the local flow field can be parameterized by the Stokes number (the dimensionless particle response time), $St = \tau_p/\tau_f$, where

$$\tau_p = \frac{2\lambda\rho_p a^2}{9\mu}\frac{\ln(\lambda+\sqrt{\lambda^2-1})}{\sqrt{\lambda^2-1}} \tag{7}$$

is a characteristic time scale of the fiber translational motion[27] with ρ_p the fiber density and $\tau_f = \nu/u^2{}_\tau$ is a characteristic time scale of near-wall turbulence. To avoid the singularity in Eqs. (5)– (7) and in the expressions for the shape factors α_0, β_0, and γ_0 in Eq. (6) when $\lambda = 1$, the simulations for spherical particles were actually performed imposing $\lambda = 1.001$.

TABLE I. Domain size and discretization for the different Reynolds numbers considered in this study. The entries for the wall-normal grid spacing Δz^+ refer to the smallest mesh size next to the solid walls and the largest grid spacing in the center of the channel.

Re	Domain size	Grid points	Δx^+	Δy^+	Δz^+	Code
150	4πh × 2πh × 2h	128 × 128 × 129	14.72	7.36	0.045−3.68	UUD[28]
180	12h × 6h × 2h	192 × 192 × 192	11.25	5.63	0.44−2.86	NTNU[20]
300	4πh × 2πh × 2h	256 × 256 × 257	14.8	7.4	0.0226−3.68	UUD[28]

III. SUMMARY OF SIMULATIONS

Direct numerical simulations of turbulent plane Poiseuille flow are performed at three different Reynolds numbers using two independent flow solvers: The UUD-solver, described in detail by Soldati and Marchioli,[28] and the NTNU-solver, described by Mortensen *et al.*[20] Both flow solvers use a pseudo-spectral method in the two homogeneous directions. In the wall-normal direction, the UUD-solver uses a Chebyshev-collocation method, whereas the NTNU-solver uses a second-order finite-difference discretization. The time integration is achieved by means of an explicit second-order Adams-Bashforth scheme. The reference geometry consists of two infinite flat parallel walls separated by a distance $2h$. Periodic boundary conditions are used in the x- and y-directions and no-slip conditions are imposed at the walls. The size of the computational domain, the number of grid nodes, and the grid spacings are provided in Table I.

We tracked swarms of 200 000 fibers with different aspect ratios ($\lambda = 1$, 3, 10, and 50) and all with Stokes number ($St = 1$, 5, 30, and 100) for a total of 16 cases for each value of Re_τ. The relevant fiber simulation parameters are summarized in Table II. The fiber tracking in the UUD solver is based on a fourth-order Runge-Kutta scheme and the fluid velocities at fiber position are obtained using sixth-order Lagrangian polynomials. The NTNU solver integrates the fiber equations of motion in time via a second-order Adams-Bashforth scheme and the local fluid velocities are interpolated with second-order accuracy. The same interpolation schemes are used to obtain the local fluid velocity gradients required in Eq. (6) for the rate-of-strain and rate-of-rotation at the fiber position.

The fiber-wall collision is fully elastic so that a fiber keeps its linear momentum in the two homogenous directions as well as its angular momentum upon touching the wall. A collision occurs every time the distance from the center of mass of a fiber, G, to the closest wall becomes less than the semi-minor axis, a. The same approach was adopted by Marchioli *et al.*[22] and by Zhang *et al.*,[21] whereas Mortensen *et al.*[20] detect collisions when G hits the wall.

All results but those presented in Sec. IV D refer to the case $Re_\tau = 150$ (see Table I). The statistics were collected over a time window $\Delta t^+ = 5100$ starting at time $t^+ = 3000$ after fiber injection. Within this time window the slip velocity statistics are at steady state whereas the fiber concentration and transport fluxes are not, at least for the fiber sets with smaller St (see, e.g., Ref. 29). All results were compared with corresponding ones collected at $Re_\tau = 180$ over a time window $\Delta t^+ = 3600$ starting at time $t^+ = 7200$ after fiber injection, and no significant quantitative differences were observed.

TABLE II. Fiber simulation parameters: All fiber sets have the same semi-minor axis $a^+ = 0.36$.

	Density ratio			
	St			
λ	1	5	30	100
1	34.72	173.60	1041.70	3472.33
3	18.57	92.90	557.10	1857.00
10	11.54	57.70	346.30	1154.33
50	7.54	37.69	226.15	753.83

The Lagrangian approach described in Sec. II B is essentially a straightforward extension to fiber-like particles of the pointwise approach routinely used for dilute suspensions of spherical particles. The reader is referred to Eaton[30] and Balachandar and Eaton[31] for comprehensive reviews of the approach. Due to its simplicity and relatively low computational cost (compared to finite-size particle computations, for instance), this approach is still widely used to simulate two-phase flows in which the collective behavior of large ensembles of particles ($\mathcal{O}(10^6)$) must be taken into account. However, it also has several important limitations, especially when applied to non-spherical particles.

First, the point-particle approach is based on the assumption that the suspended particles are smaller than the smallest scales of the fluid flow. In turbulent flows these scales are of order of the Kolmogorov length η since variations over shorter distances are prohibited by the action of viscous diffusion. The diameter of a spherical particle should therefore be smaller than η. Similarly, the length $2b$ of the prolate spheroids should not exceed η. This condition may be difficult to meet when spheroids with significant elongation (mimicking fibers) are considered: as the aspect ratio increases, the length $2b$ can become larger than η, and also larger than the grid size (even though the "diameter" $2a$ does not). Accordingly, the fluid velocity and the fluid velocity gradients may vary along the fiber, thus violating assumptions inherent in the point-particle approach.

Even if the particles are sufficiently small compared with the scales of the flow, a further requirement is that their Reynolds number be smaller than one. This constraint is associated with the use of the analytically derived expressions for the force, Eq. (4), and torque, Eq. (6), that are acting on the fiber particle. These expressions are based on the assumption that the flow around the particle is Stokesian so that fluid inertia can be ignored. Several correction formulas exist to account for finite-Reynolds-number effects on the motion of spherical particles but, as mentioned in Sec. II B, no such corrections yet exist for non-spherical particles.

Another limitation is concerned with currently available wall-collision models, based solely on the distance of the center of mass relative to the wall. These models, used in connection with Jeffery equations (which are not valid in close neighborhood of a rigid wall and therefore are not bound to obey geometrical constraints), are probably inadequate since they allow kinematically impossible orientation states. This inadequacy may show up especially for high-aspect-ratio particles, which may touch the wall even though their center of mass is still fairly far away from it.

In addition to the above-mentioned issues, another simplification adopted in this study (as in most Lagrangian particle tracking simulations) is the neglect of particle-particle collisions. This choice could readily be justified for sufficiently dilute suspensions according to the flow regime map provided by Elghobashi,[32] with the caveat that the validity of this map for non-spherical particles is probably questionable (but no alternative has been proposed so far).

To summarize, we believe that the point-particle approach as described in Sec. II B is a realistic representation of fiber-like particles provided that both particle inertia and length are modest. Otherwise, the shortcomings discussed in this paragraph may not be disregarded. As far as the present results are concerned, this implies that those presented for the heaviest ($\mathrm{St} = 100$) and longest ($\lambda = 50$) fibers should be considered to highlight trends in the (St, λ) parameter space, not to provide exact quantitative predictions.

IV. RESULTS AND DISCUSSIONS

The slip velocity is largely dependent on the distance from the wall, z^+, as shown by Zhao *et al.*,[19] for instance. Let us first, however, decompose the instantaneous slip velocity vector $\Delta\mathbf{u}$ into a mean

$$\langle \Delta\mathbf{u}(z) \rangle = \langle \mathbf{u}_f \rangle - \langle \mathbf{u}_p \rangle, \tag{8}$$

and a fluctuating part

$$\Delta\mathbf{u}'(z) = \mathbf{u}'_f - \mathbf{u}'_p \tag{9}$$

with $\mathbf{u}_f = \langle \mathbf{u}_f \rangle + \mathbf{u}'_f$ and $\mathbf{u}_p = \langle \mathbf{u}_p \rangle + \mathbf{u}'_p$. Brackets denote the quantities evaluated at fiber positions and averaged in the two homogeneous directions and in time.

A. Fiber preferential distribution and slip velocity in low/high speed streaks

It is well known that the magnitude of the turbulent velocity fluctuations reaches a maximum value in the buffer layer where the turbulence is characterized by strong ejections and sweeps, e.g., Kim *et al.*[33] Transport, clustering, and deposition of small spherical particles in the near-wall region have been widely investigated and strong and complex particle-turbulence interactions have been reported.[28,31,34–41] The maximum value of the streamwise slip velocity was observed in the buffer layer by Zhao *et al.*[19] In present study, the first part of results (Figures 1–12) focuses on the effects of fiber aspect ratio and fiber inertia on the fiber clustering and the instantaneous slip velocity fluctuations $\mathbf{\Delta u'}$ in a wall-parallel (x, y)-plane at $z^+ = 8$. This particular position is chosen as the wall-distance at which the magnitudes of the mean slip velocity and the slip velocity fluctuations reach a maximum for spherical particles.[19] Therefore it appears adequate to highlight near-wall (anisotropic) effects on the relative motion between fibers and fluid.

The snapshots in Figures 1 and 2 give a first impression of the instantaneous fiber behavior in the near-wall region. The gray-scale contours represent the streamwise fluid velocity fluctuations $u' = u - U$, where u and U are instantaneous and mean values of the streamwise component of the fluid velocity vector at the grid nodes. The streaky nature of the flow in the near-wall region is clearly visualized as elongated regions of low-speed fluid (dark areas) alternating with regions of fast-moving fluid (light areas).

The plots in Figure 1 show the tendency that fibers with $St = 30$ but different aspect ratio avoid the high-speed regions and concentrate in the low-speed regions even though not the regions with the slowest-moving fluid. The fibers are evidently not distributed evenly across the wall-parallel (x, y)-plane and there is no distinct influence of the fiber aspect ratio λ. The ability of inertial spheres ($\lambda = 1$) to distribute themselves unevenly is consistent with earlier observations by Fessler *et al.*,[36] and by Marchioli and Soldati.[34] They reported a tendency of spheres to preferentially concentrate in the low-speed streaks.

The fibers are colored by the instantaneous slip-velocity Δu^+ in the streamwise direction. Irrespective of aspect ratio, there is a tendency that fibers position themselves in a tandem arrangement with several fibers in a row.[20,22,42] The fibers in these long rows all have $\Delta u^+ > 0$, i.e., they are dragged forward by the faster-moving fluid.

The snapshots in Figure 2 demonstrate the effect of inertia on the tendency of the $\lambda = 10$ fibers to segregate near the wall. The lightest fibers ($St = 1$) concentrate almost randomly in Figure 2(a). The fibers seem to distribute more evenly than at $St = 30$ and with higher concentrations for the highest Stokes number. Moreover, fibers with both positive and negative slip velocities are found in the low-speed regions. There is a tendency that the magnitude of the particle slip velocity Δu^+ increases with St and the number of fibers with positive slip velocity (red color online) seems to exceed the number of fibers with negative slip velocity (blue color online). This suggests that a larger proportion of fibers moves slower than the local fluid and thus is accelerated in the streamwise direction by the Stokes force. The qualitative observations drawn from the instantaneous plots in Figures 1 and 2 will be substantiated by means of statistical analysis in the following.

To quantitatively analyze the role of the fiber-slip velocity in near-wall turbulence, we examine first the conditioned probability density functions of the streamwise fluid velocity fluctuations, PDF(u'_f), shown in Figures 3 and 4. In these two figures, as well as in Figs. 9–12, superscript + has been dropped to simplify the notation. The two PDFs in each plot are conditioned on positive (solid line) and negative (dotted line) streamwise slip velocity values, respectively, and are normalized to yield a total area (sum of the area under the curves) equal to unity. It is already known that $\langle \Delta u \rangle^+$ attains a negative peak near $z^+ = 8$.[19] This implies $\langle u_p \rangle^+ > \langle u_f \rangle^+$. Moreover, the fluid velocity seen by the particles $\langle u_f \rangle^+$ is lower than the Reynolds-averaged fluid velocity U. This phenomenon is well-known for spherical particles and was recently shown also for elongated particles by Mortensen *et al.*[20] The observation that $\langle u_f \rangle^+$ is lower than U in the buffer region of a turbulent wall flow is generally ascribed to preferential concentration in low-speed streaks.[34]

The different PDFs for St = 30 fibers in the four panels of Figure 3 are almost indistinguishable. The elongation of the fibers does not seem to play an important role on the spatial distribution of fibers in a near-wall layer, thus confirming the qualitative observations drawn from Figure 1. It is

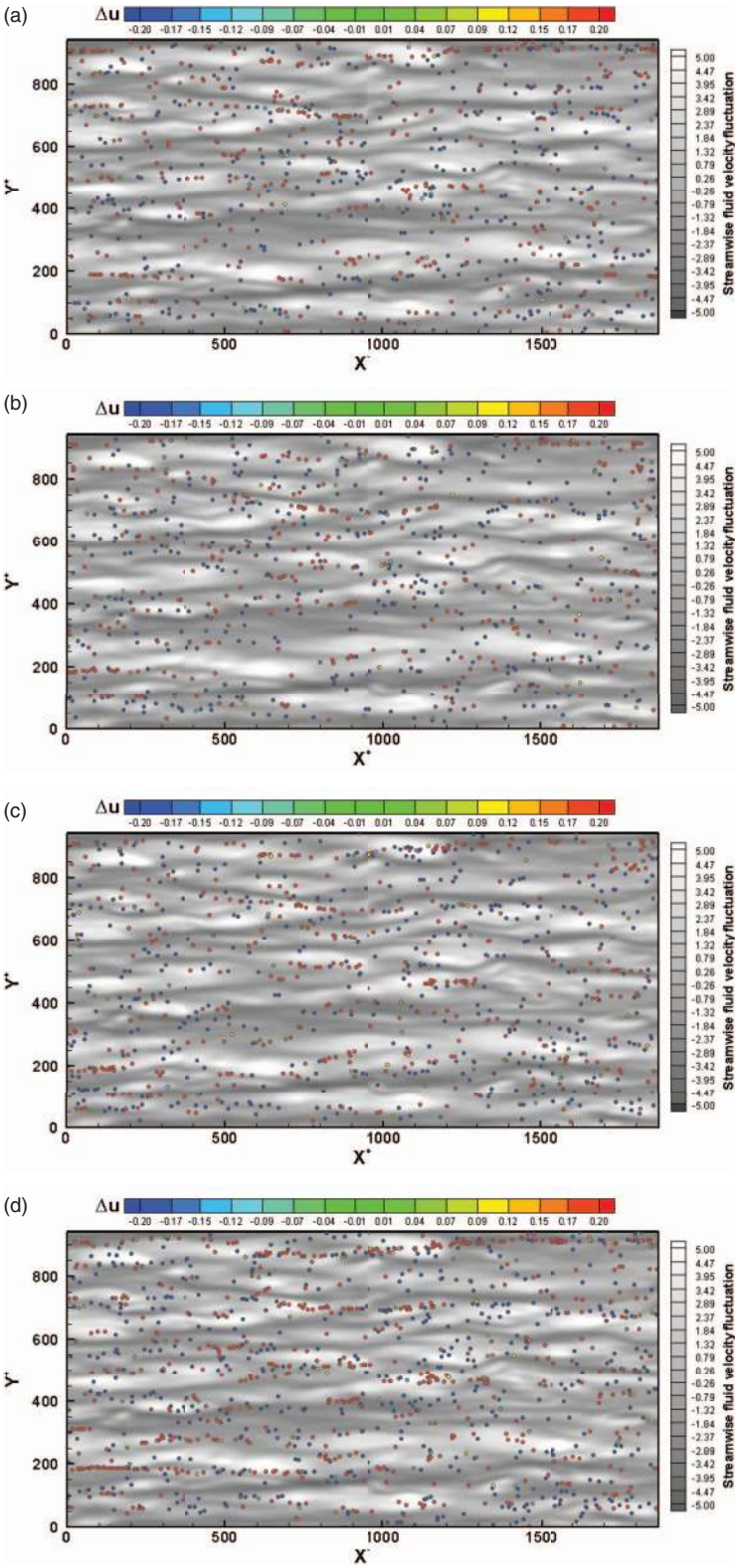

FIG. 1. Instantaneous streamwise slip velocity, Δu^+, and $St = 30$ fiber distribution in the wall-parallel x-y plane taken at $z^+ \simeq 8$. Fibers are colored according to the value of Δu^+ at their location: red/blue indicate fibers with large positive/negative slip velocity. The near-wall fluid velocity streaks (represented as gray-scale iso-contours of the streamwise fluid velocity fluctuation, u') are also shown. Panels: (a) $\lambda = 1$, (b) $\lambda = 3$, (c) $\lambda = 10$, and (d) $\lambda = 50$.

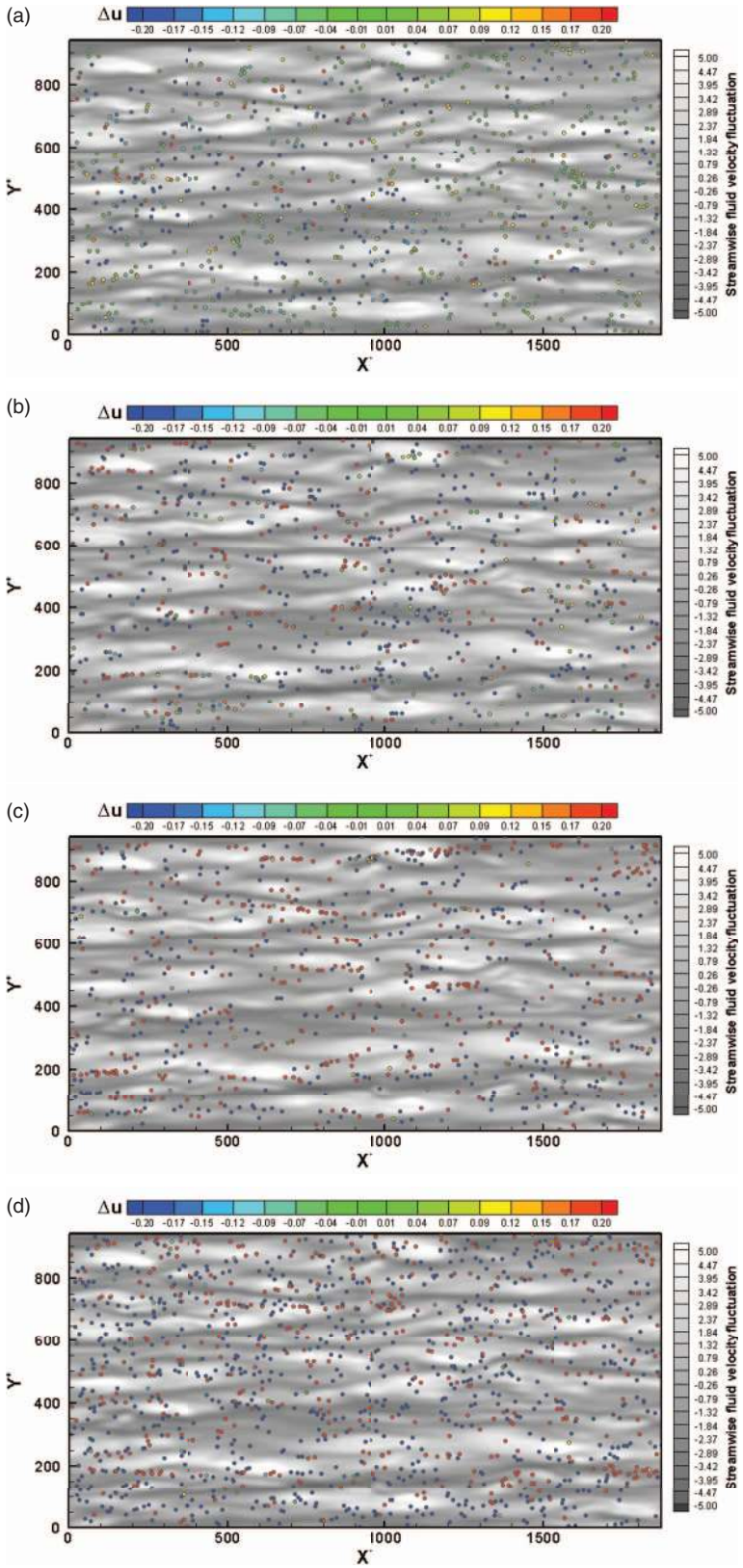

FIG. 2. Instantaneous streamwise slip velocity, Δu^+, and $\lambda = 10$ fiber distribution in the wall-parallel x-y plane taken at $z^+ \simeq 8$. Color codes are as in Fig. 1. Panels: (a) $St = 1$, (b) $St = 5$, (c) $St = 30$, and (d) $St = 100$.

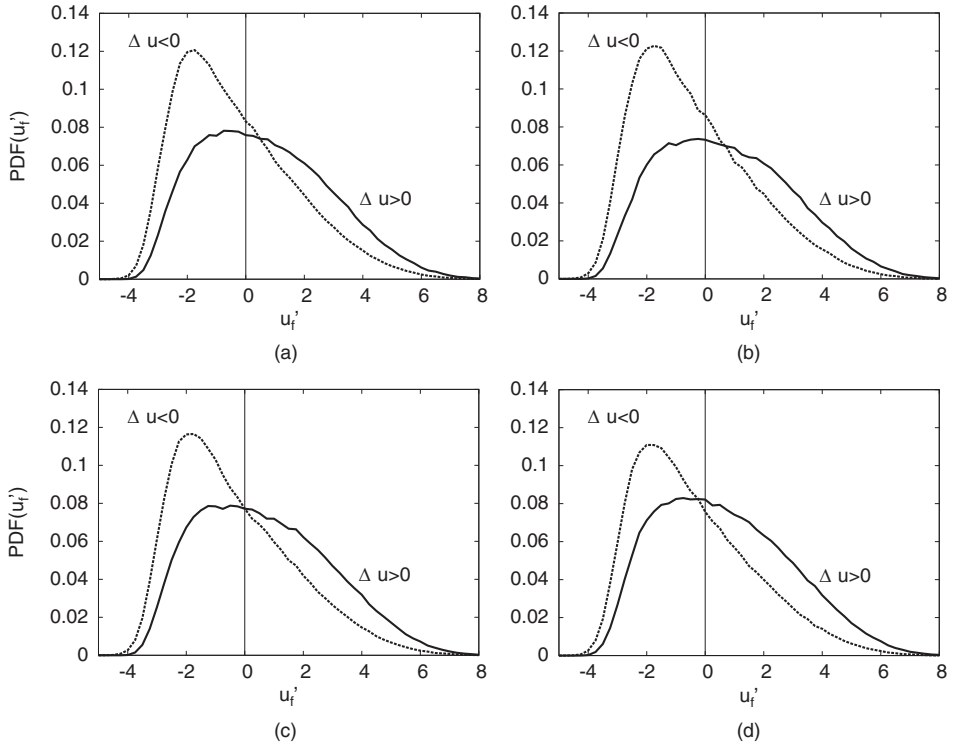

FIG. 3. Effect of fiber elongation on conditioned PDF(u'_f) for the reference case of fibers with $St = 30$. Solid (dashed) lines refer to the PDF computed for fibers with $\Delta u > 0$ ($\Delta u < 0$). Panels: (a) $\lambda = 1$; (b) $\lambda = 3$; (c) $\lambda = 10$; and (d) $\lambda = 50$.

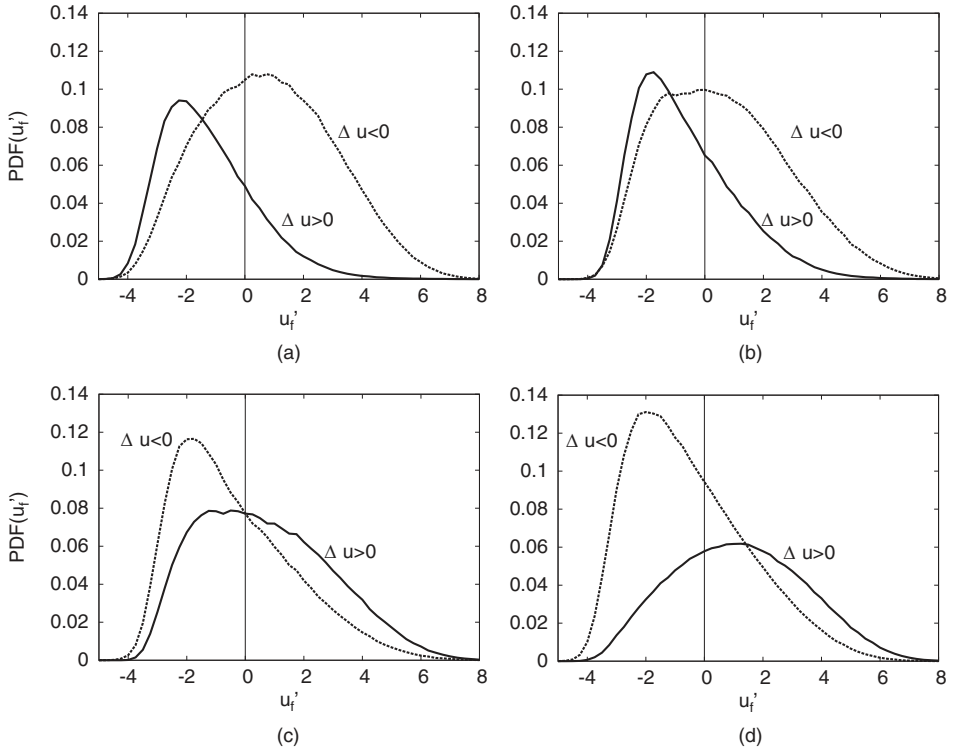

FIG. 4. Effect of fiber inertia on conditioned PDF(u'_f) for the reference case of fibers with $\lambda = 10$. Panels: (a) $St = 1$; (b) $St = 5$; (c) $St = 30$; and (d) $St = 100$. Lines are as in Fig. 3.

generally observed that both PDFs are skewed with their peak in the $u'_f < 0$ semi-plane, i.e., in areas where the local fluid velocity is lower than mean fluid velocity seen by the particles. Since $\langle u_f \rangle^+$ is lower than U in the buffer region, $u'_f < 0$ definitely represents a low-speed area.

However, the PDFs obtained with fixed aspect ratio ($\lambda = 10$) reveal a distinct effect of inertia, shown in Figure 4. The lightest fibers ($St = 1$) are not totally randomly distributed, as already suggested by Figure 2(a): Figure 4(a) shows a preferential concentration of fibers with positive slip velocity $\Delta u^+ > 0$ in low-speed regions with a peak value of PDF(u'_f) located at $u'_f \simeq -2$. Fibers with $\Delta u^+ < 0$, on the other hand, exhibit a more symmetric distribution that peaks towards slightly positive u'_f values.

With increasing fiber inertia, the PDFs conditioned on $\Delta u^+ < 0$ become skewed towards the low-speed region, whereas the PDFs conditioned on $\Delta u^+ > 0$ shift gradually towards relatively high-speed regions. This shift is evident for the two most inertial fiber sets. The PDFs for the $St = 100$ fibers, in particular, are both qualitatively and quantitatively different from the fibers with least inertia. Like spherical particles, it is believed that fibers are convected from the core region towards the wall by strong sweeping events.[20] The most inertial fibers apparently retain their streamwise momentum from the faster moving core region and accordingly move faster than the local fluid, i.e., $\Delta u^+ < 0$, in the low-speed streaks.

B. Fiber slip velocity in sweeps and ejections

Marchioli and Soldati[34] described how effectively spherical particles were transported towards and away from a solid wall by means of sweeps and ejections. In order to investigate how sweeps and ejections determine fiber transport, the streamwise and wall-normal components of the slip velocity vector have been conditioned on ejection and sweep events in Figures 5–8, i.e., on whether the observation is in the second (Q2) or the fourth (Q4) quadrant of a w'_f versus u'_f diagram, where w'_f represents the fluid velocity fluctuations in the wall-normal direction. We remark here that the use of Lagrangian conditioned velocities makes the present quadrant analysis quantitatively different from the standard approach in which Eulerian velocities are considered and ejections and sweeps events are associated with the second and fourth quadrants in a w' versus u' plot.[33,43] This is because, due to the preferential concentration of inertial fibers, w'_f and u'_f are generally different from w' and u'.

The probability density functions, PDF(Δu^+), conditioned on Q2−events (dotted lines) appear almost unaffected by the aspect ratio of the fibers, as shown in Figure 5. The PDFs, which refer to $St = 30$ fibers, are slightly skewed with the peak at small positive Δu^+, and only the magnitude of this peak changes non-monotonically with λ. The PDFs conditioned on Q4−events are also centered at positive slip velocities and exhibit a more evident λ−effect. The $St = 30$ fibers, no matter if entrained in sweep or ejection events, move slower than the local fluid in the streamwise direction. This observation is consistent with the instantaneous plots in Figure 1 which suggested that the number of fibers with $\Delta u^+ > 0$ exceeds the number of fibers with $\Delta u^+ < 0$. Compared with spherical particles in Figure 5(a), the PDFs for the $\lambda = 10$ fibers in Figure 5(c) show that a larger number of fibers are involved with ejection events whereas the number of fibers in sweep events is reduced.

The moderately long fibers with $\lambda = 10$ and modest inertia ($St = 1$ and 5, Figures 6(a) and 6(b)) seem to passively follow the sweeps. The PDF(Δu^+) conditioned on Q4−events (solid lines) is almost perfectly symmetric about $\Delta u^+ = 0$ and shows a relatively narrow range of slip velocity values, indicating that fibers follow closely the fluid. With increasing inertia, however, the peak is shifted monotonically towards positive Δu^+ indicating that fibers tend to lag the fluid when trapped inside sweep events. The Stokes number effect on the slightly skewed PDF(Δu^+) conditioned on Q2−events (dotted line) is also noticeable: as St increases the peak value is gradually reduced and the PDFs become broader, covering a wider range of Δu^+ values. Overall, Figs. 5 and 6 show that the PDFs of Δu^+ can not be approximated by Gaussian functions. This finding provides indirect evidence of the intermittency of fiber translational motion in non-homogeneous anisotropic turbulence, and has implications for the modelling because it suggests that fiber motion relative to the fluid can be treated as a diffusion process[44] with non-constant diffusion coefficient (not a standard Ornstein-Uhlenbeck process therefore). As in many other physical applications, one may

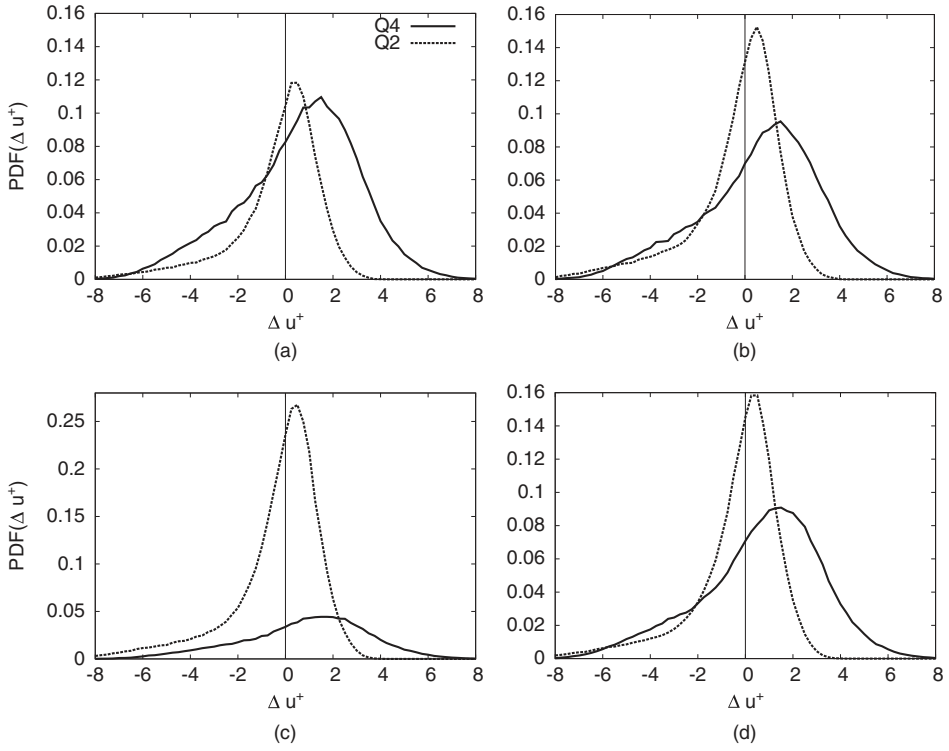

FIG. 5. Effect of fiber elongation on conditioned PDF(Δu^+) for the reference case of fibers with $St = 30$. Panels: (a) $\lambda = 1$; (b) $\lambda = 3$; (c) $\lambda = 10$; and (d) $\lambda = 50$. Solid lines and dashed lines refer to the PDF computed for fibers within sweeps (Q4 events with $u'_f > 0$ and $w'_f < 0$) and ejections (Q2 events with $u'_f < 0$ and $w'_f > 0$), respectively.

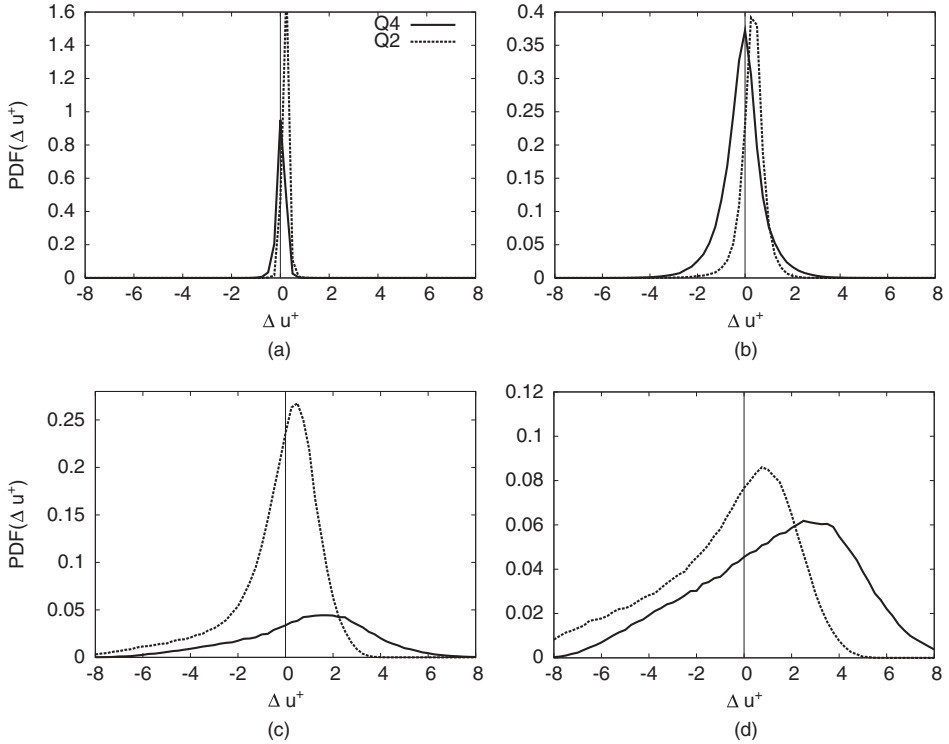

FIG. 6. Effect of fiber inertia on conditioned PDF(Δu^+) for the reference case of fibers with $\lambda = 10$. Panels: (a) $St = 1$; (b) $St = 5$; (c) $St = 30$; and (d) $St = 100$. Lines are as in Fig. 5.

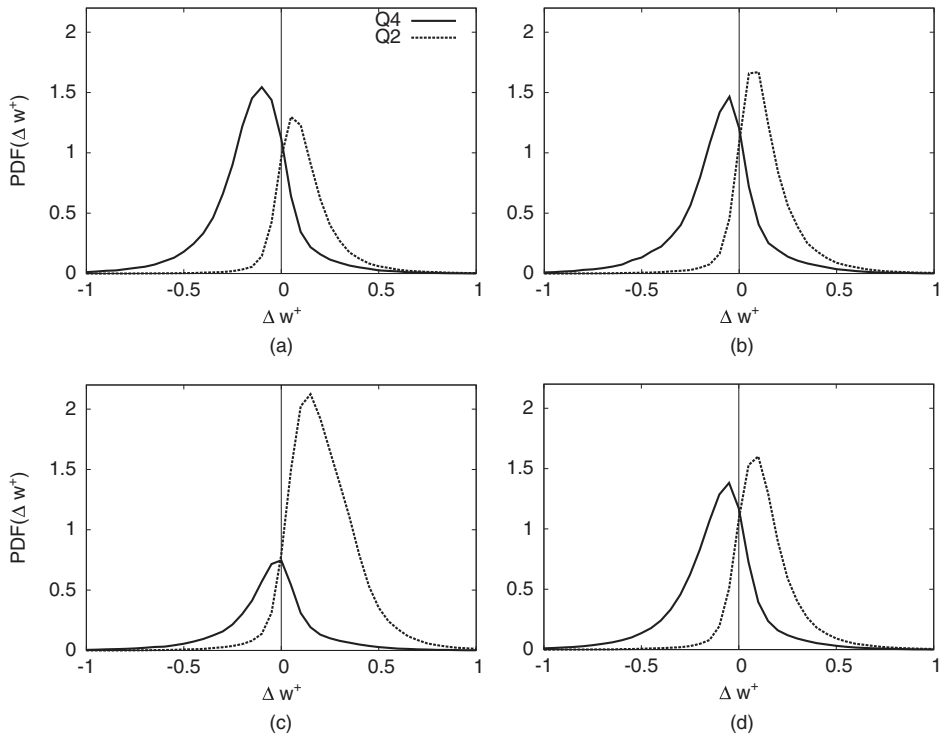

FIG. 7. Effect of fiber elongation on conditioned PDF(Δw^+) for the reference case of fibers with $St = 30$. Panels: (a) $\lambda = 1$; (b) $\lambda = 3$; (c) $\lambda = 10$; and (d) $\lambda = 50$. Lines are as in Fig. 5.

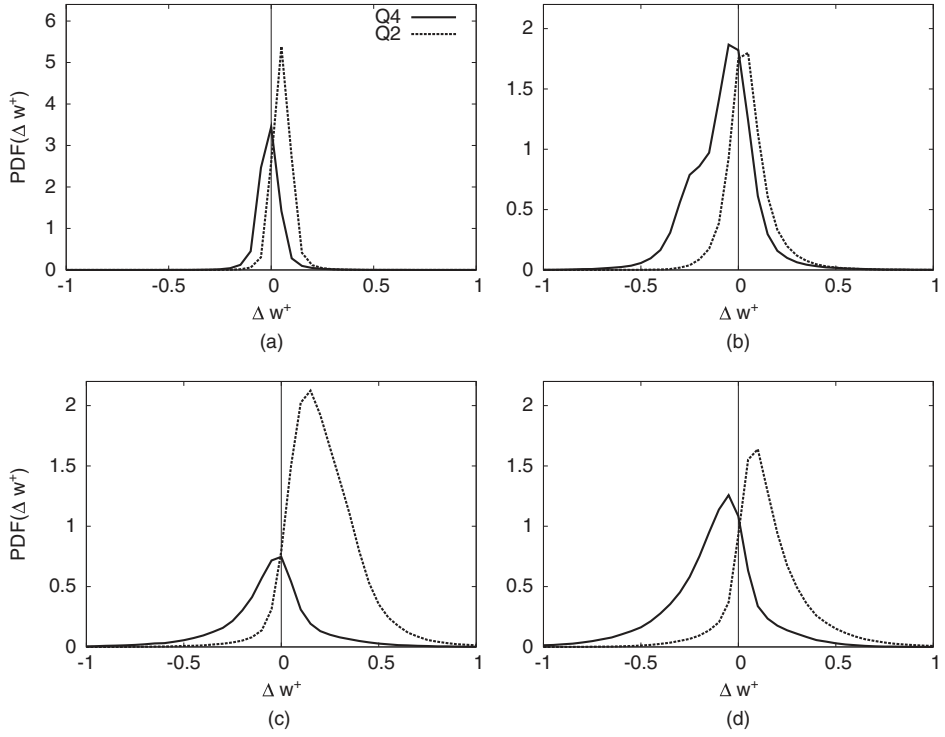

FIG. 8. Effect of fiber inertia on conditioned PDF(Δw^+) for the reference case of fibers with $\lambda = 10$. Panels: (a) $St = 1$; (b) $St = 5$; (c) $St = 30$; and (d) $St = 100$. Lines are as in Fig. 5.

need to consider a diffusion coefficient that is not just a function of the value of the process but also a function of its averages.[45,46]

The probability density functions of the wall-normal slip velocity PDF(Δw^+) are presented in Figures 7 and 8. Δw^+ is undoubtedly an essential quantity with respect to fiber transport towards the wall. For $St = 30$, the PDFs conditioned on sweeps (ejections) peak at a negative (positive) Δw^+. This observation implies that the fibers are moving slower than the surrounding fluid also in the wall-normal direction, irrespective of whether they are carried along by an ejection or a sweep.

When inertial effects are considered in Figure 8, the distribution function PDF(Δw^+) conditioned on sweep events (solid lines) shifts its peak from zero to slightly negative values of Δw^+ as the Stokes number is increased from 1 to 100. On the other hand, the PDFs conditioned on ejections (dotted lines) always peak in the $\Delta w^+ > 0$ semi-plane, with just a slight shift towards higher positive values at increasing St. Note that PDF(Δw^+) exhibits very small differences for long fibers with high inertia, as can be noticed from comparison of Figs. 7(d) and 8(d), which are in turn very similar to the PDF obtained for the fiber set with $\lambda = 50$ and $St = 100$ (not shown). This indicates that the relative fiber-fluid motion becomes independent of elongation and inertia for sufficiently high λ and St. As far as λ is concerned, present results are in agreement with the observations of Manhart,[47] who argued that the aspect ratio λ of long rods does not affect the qualitative behavior of the particle stresses as long as $\lambda \geq 100$. Similar findings have been reported more recently by Zhao *et al.*[48] for fibers with $\lambda = 500$.

Let us now examine how the sign of the slip velocity fluctuations $\Delta u'$ correlates with the sign of the fluctuations of the fluid velocity at the particle position u'_f. For the sake of brevity only fluctuations in the streamwise direction are considered in Figures 9 and 10. Each of the scatter plots in Figures 9 and 10 (as well as in the subsequent Figures 11 and 12) shows instantaneous data, i.e., points, taken at discrete intervals of 100 t^+ and accumulated over the same time window considered for averaging the slip velocity statistics (thus accounting for a total of 51 samples). The scatter plots for $St = 30$ fibers show a distinctly asymmetric distribution in the ($\Delta u'$, u'_f)−plane. It is particularly noteworthy that large positive slip velocities never coincide with large negative fluid velocity fluctuations. Nevertheless, the number of events in the second quadrant (Q2) is roughly the same as the number of Q1 and Q3 events, whereas Q4 events ($\Delta u' < 0$, $u'_f > 0$), which correspond to highly intermittent fiber-to-fluid motions in high-speed regions, are by far less frequent. It can furthermore be observed that the fraction of events with negative fluid velocity, i.e., the sum of Q2 and Q3 events, accounts for more than 55% of the total. This observation again suggests that the fibers tend to concentrate preferentially in low-speed streaks. It is remarkable that these findings are valid irrespective of the shape of the particle, i.e., for the spherical particles in Figure 9(a) as well as for the elongated fibers in Figures 9(b)–9(d).

Scatter plots for $\lambda = 10$ particles are presented in Figure 10 to demonstrate the effect of particle inertia. It is readily seen that the distribution in the ($\Delta u'$, u'_f)-plane is substantially affected by the Stokes number and the range of the slip velocity fluctuations increases for the more inertial fibers. This observation is consistent with a similar finding for spherical particles by Zhao *et al.*,[19] namely, that the standard deviation of the streamwise slip velocity fluctuations increase monotonically with St. The results in Figure 10 show that both the number of Q1 and Q3 events increases with increasing Stokes numbers, whereas the number of Q2 and Q4 events is correspondingly reduced. Nevertheless, the sum of Q2 and Q3 events accounts for somewhat more than 55% of the total, irrespective of the actual Stokes number. For the sake of completeness, an overview of statistical data from the quadrant analysis of all 16 particle classes is provided in Table III.

Scatter plots corresponding to those in Figures 9 and 10 are presented in Figures 11 and 12, but now with the view to see how the slip velocity fluctuations $\Delta u'$ correlate with the particle velocity fluctuations u'_p. The scatter plots for St = 30 particles in Figure 11 show a distinctly different distribution in the ($\Delta u'$, u'_p)-plane than the correlation between $\Delta u'$ and u'_f in Figure 9. Now it is observed that large negative slip velocities never co-exist with large negative particle velocity fluctuations. The fractions of the number of events in each of the four quadrants are almost unaffected by the fiber elongation over the aspect ratio range from 1 to 50. It is noteworthy that about 70% of the events, i.e., Q2 and Q4, contribute to a negative correlation between $\Delta u'$ and u'_p as we shall see later.

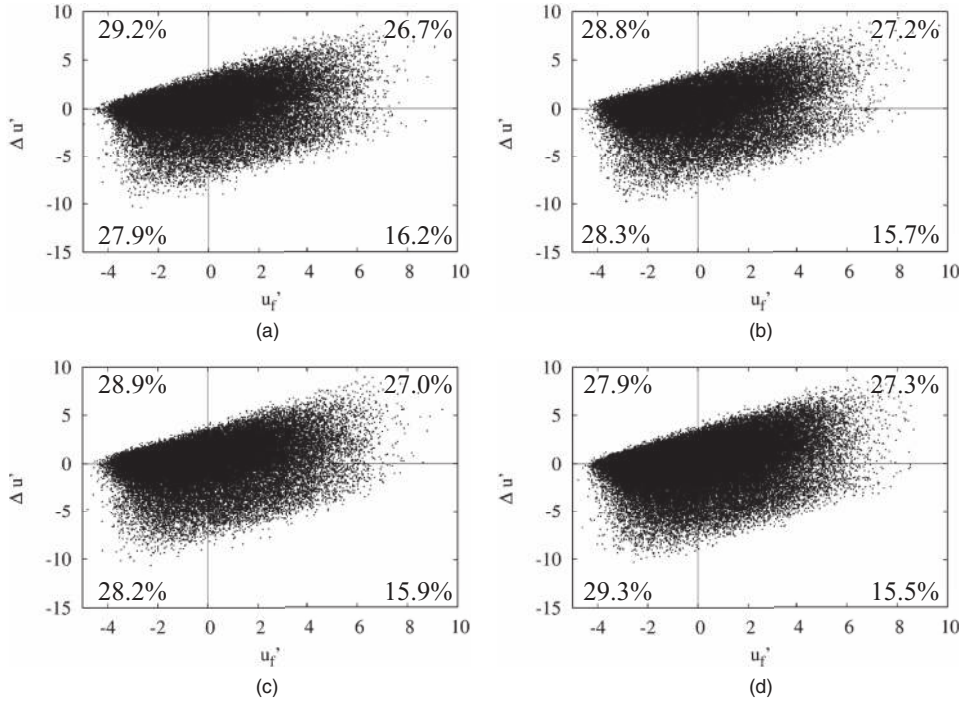

FIG. 9. Effect of fiber elongation on the scatter plots of the fluid and slip velocity fluctuations, u'_f and $\Delta u'$ respectively, conditionally sampled at the $St = 30$ fiber positions. For comparison purposes, percent values corresponding to the number of fibers in each quadrant are provided in Table III. Panels: (a) $\lambda = 1$; (b) $\lambda = 3$; (c) $\lambda = 10$; and (d) $\lambda = 50$.

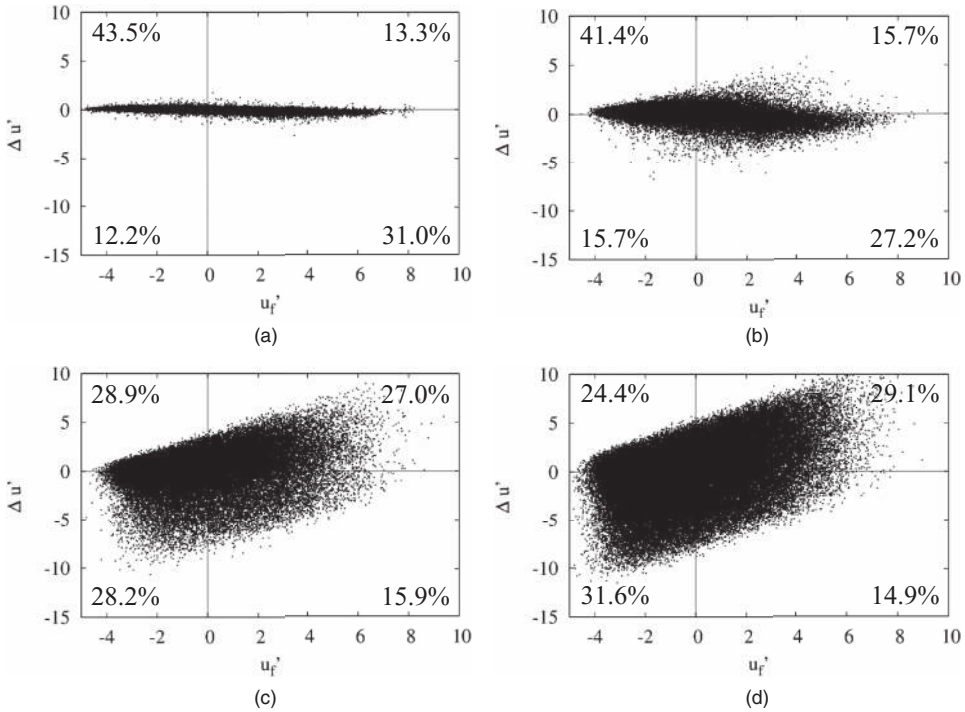

FIG. 10. Effect of fiber inertia on the scatter plots of the fluid and slip velocity fluctuations, u'_f and $\Delta u'$ respectively, conditionally sampled at the $\lambda = 10$ fiber positions. For comparison purposes, percent values corresponding to the number of fibers in each quadrant are provided in Table III. Panels: (a) $St = 1$; (b) $St = 5$; (c) $St = 30$; and (d) $St = 100$.

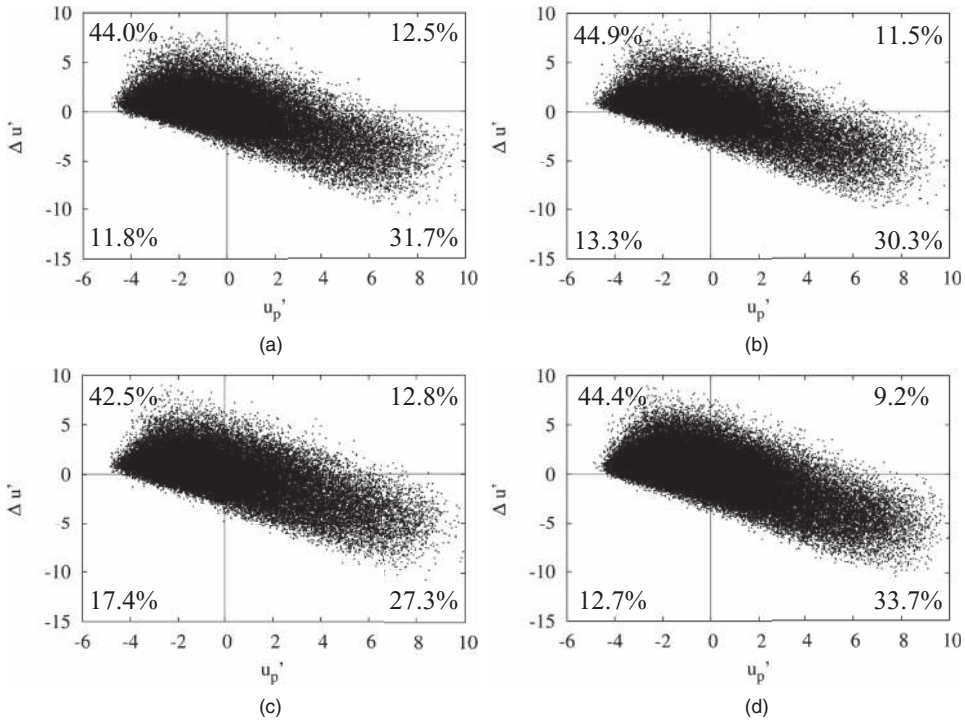

FIG. 11. Effect of fiber elongation on the scatter plots of the fiber and slip fluctuations, u'_p and $\Delta u'$, respectively, conditionally sampled at the $St = 30$ fiber positions. For comparison purposes, percent values corresponding to the number of fibers in each quadrant are provided in Table III. Panels: (a) $\lambda = 1$; (b) $\lambda = 3$; (c) $\lambda = 10$; and (d) $\lambda = 50$.

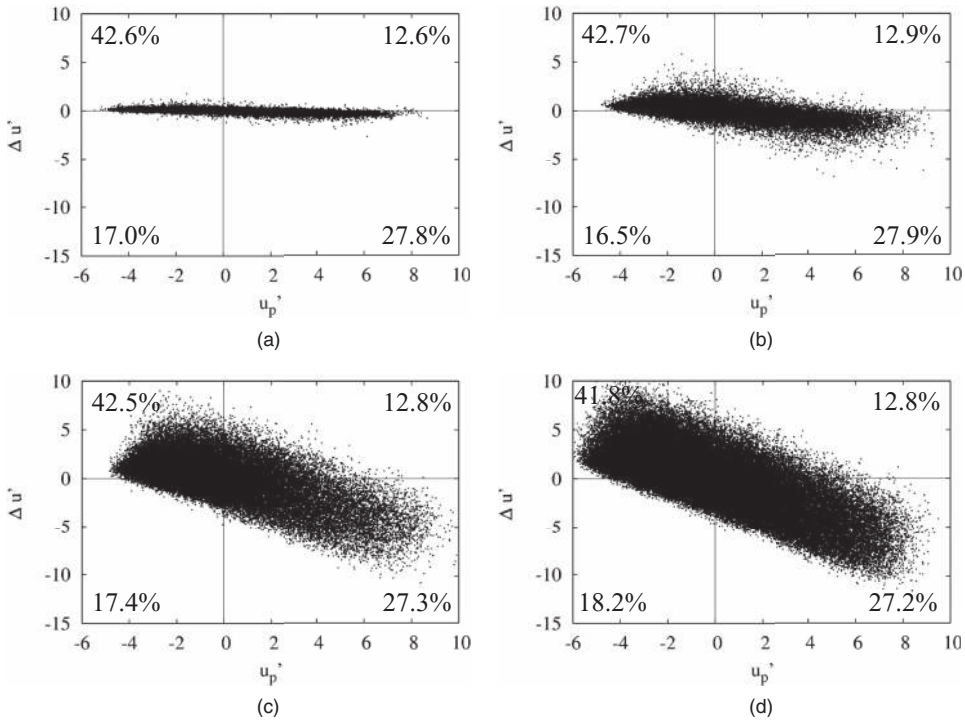

FIG. 12. Effect of fiber inertia on the scatter plots of the fiber and slip fluctuations, u'_p and $\Delta u'$, respectively, conditionally sampled at the $\lambda = 10$ fiber positions. For comparison purposes, percent values corresponding to the number of fibers in each quadrant are provided in Table III. Panels: (a) $St = 1$; (b) $St = 5$; (c) $St = 30$; and (d) $St = 100$.

TABLE III. Percent fiber counts for each (u'_f, $\Delta u'$) quadrant at varying fiber inertia and elongation. See also Figs. 9 and 10.

	II quadrant					I quadrant			
	St					*St*			
λ	1	5	**30**	100	λ	1	5	**30**	100
1	43.6	41.4	**29.2**	24.1	1	13.1	15.8	**26.7**	29.7
3	43.6	41.5	**28.8**	24.4	3	13.1	15.8	**27.2**	29.3
10	**43.5**	**41.4**	**28.9**	**24.4**	**10**	**13.3**	**15.7**	**27.0**	**29.1**
50	43.0	41.3	**27.9**	24.4	50	13.0	15.3	**27.3**	29.1
	III quadrant					IV quadrant			
	St					*St*			
λ	1	5	**30**	100	λ	1	5	**30**	100
1	12.1	15.5	**27.9**	31.7	1	31.2	27.3	**16.2**	14.5
3	12.2	15.4	**28.3**	31.6	3	31.1	27.3	**15.7**	14.8
10	**12.2**	**15.7**	**28.2**	**31.6**	**10**	**31.0**	**27.2**	**15.9**	**14.9**
50	12.6	15.8	**29.3**	31.5	50	31.4	27.6	**15.5**	15.0

The scatter plots for the particular aspect ratio $\lambda = 10$ in Figure 12 exhibit the crucial effect of particle inertia. Also here the sum of the Q2 and Q4 events amounts to 70% or even slightly more of the total and thus accounts for a negative correlation between $\Delta u'$ and u'_p irrespective of fiber inertia. Table IV provides an overview of statistical data from the quadrant analysis of all 16 particle classes examined.

C. Statistical results in the wall-normal direction

In this section, the focus is on long-time and space-averaged statistics. First of all correlations between the slip velocity and the fiber velocity in the streamwise and wall-normal directions are shown in Figures 13(a) and 13(b), respectively. These second-order correlations contribute to the work done by the local fluid to move the fibers. Similarly, the correlations between the slip velocity and the fluid velocity seen (not shown herein) contribute to the work done by the fibers on the local fluid. These correlations are responsible for the coupling between the fluid and particulate phases in two-way coupled simulations and are essential in a variety of different modelling approaches.[16,49,50] The reader is referred to the paper by Zhao, Andersson and Gillissen[51] for a detailed description of the conversion of mechanical work between spherical particles and turbulent fluid flow.

TABLE IV. Percent fiber counts for each (u'_p, $\Delta u'$) quadrant at varying fiber inertia and elongation. See also Figs. 11 and 12.

	II quadrant					I quadrant			
	St					*St*			
λ	1	5	**30**	100	λ	1	5	**30**	100
1	44.3	44.8	**42.6**	44.2	1	12.3	12.0	**12.6**	9.7
3	44.0	44.9	**42.7**	44.3	3	12.4	11.8	**12.9**	9.4
10	**44.0**	**44.9**	**42.5**	**44.4**	**10**	**12.5**	**11.5**	**12.8**	**9.2**
50	43.4	45.0	**41.8**	44.8	50	12.1	11.1	**12.8**	8.9
	III quadrant					IV quadrant			
	St					*St*			
λ	1	5	**30**	100	λ	1	5	**30**	100
1	11.5	13.0	**17.0**	13.4	1	31.9	30.2	**27.8**	32.7
3	11.7	12.8	**16.5**	12.9	3	31.8	30.5	**27.9**	33.4
10	**11.8**	**13.3**	**17.4**	**12.7**	**10**	**31.7**	**30.3**	**27.3**	**33.7**
50	12.1	13.3	**18.2**	12.7	50	32.3	30.6	**27.2**	33.6

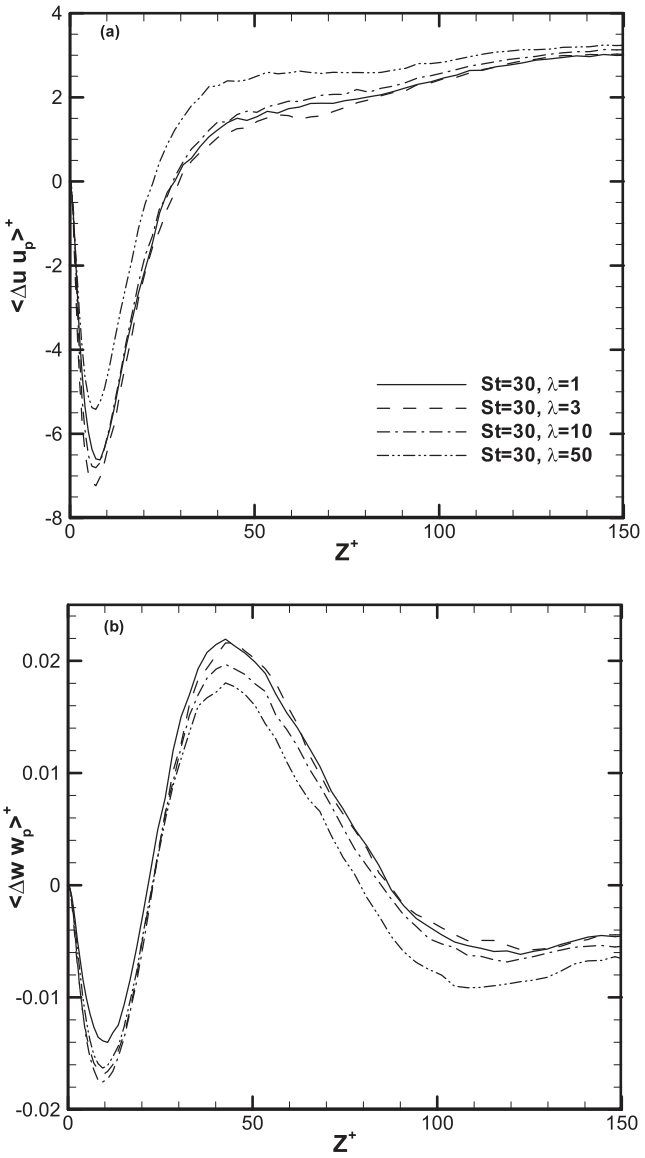

FIG. 13. Effect of fiber elongation on the work done by fluid on fibers at St = 30. Panels: (a) Streamwise work, $\langle \Delta u \cdot u_p \rangle^+$; (b) wall-normal work, $\langle \Delta w \cdot w_p \rangle^+$. Lines: ——— $\lambda = 1$, − − − $\lambda = 3$, − · − · − $\lambda = 10$, − · · − · · − $\lambda = 50$.

The correlation between the slip velocity and the particle velocity $\langle \Delta u \cdot u_p \rangle^+$ for St = 30, shown in Figure 13(a), exhibits a distinct negative peak just outside of the viscous-dominated region, at $z^+ \approx 7$. The negative correlation between Δu^+ and u_p^+ is consistent with the skewed scatter plots in Figures 11 and 12 and moreover reflects that the fibers most likely would have exerted mechanical work on the fluid throughout the viscous and buffer regions if the simulations were two-way coupled. It should be noted that $\langle \Delta u \cdot u_p \rangle^+ = \langle \Delta u' \cdot u_p' \rangle^+ + \langle \Delta u \rangle^+ \cdot \langle u_p \rangle^+$ with $\langle \Delta u \rangle^+$ being negative near the wall (as will be shown later in Figure 14) and $\langle u_p \rangle^+$ being positive throughout the channel section (particles all travel with the mean flow along the streamwise direction). The two-way coupled simulations of turbulent channel flow laden with spherical particles by Zhao *et al.*[51] showed that both $\langle \Delta u \cdot u_p \rangle^+$ and $\langle \Delta u' \cdot u_p' \rangle^+$ exhibit a distinct negative peak at $z^+ \approx 12$, and that the correlation $\langle \Delta u' \cdot u_p' \rangle^+$ contributed about 40% to the overall $\langle \Delta u \cdot u_p \rangle^+$. Further away from the wall the correlation changes sign and remains positive all the way to the channel center plane. The positive work of the fluid on the fibers beyond $z^+ \approx 30$, implies that the fibers are receiving mechanical energy

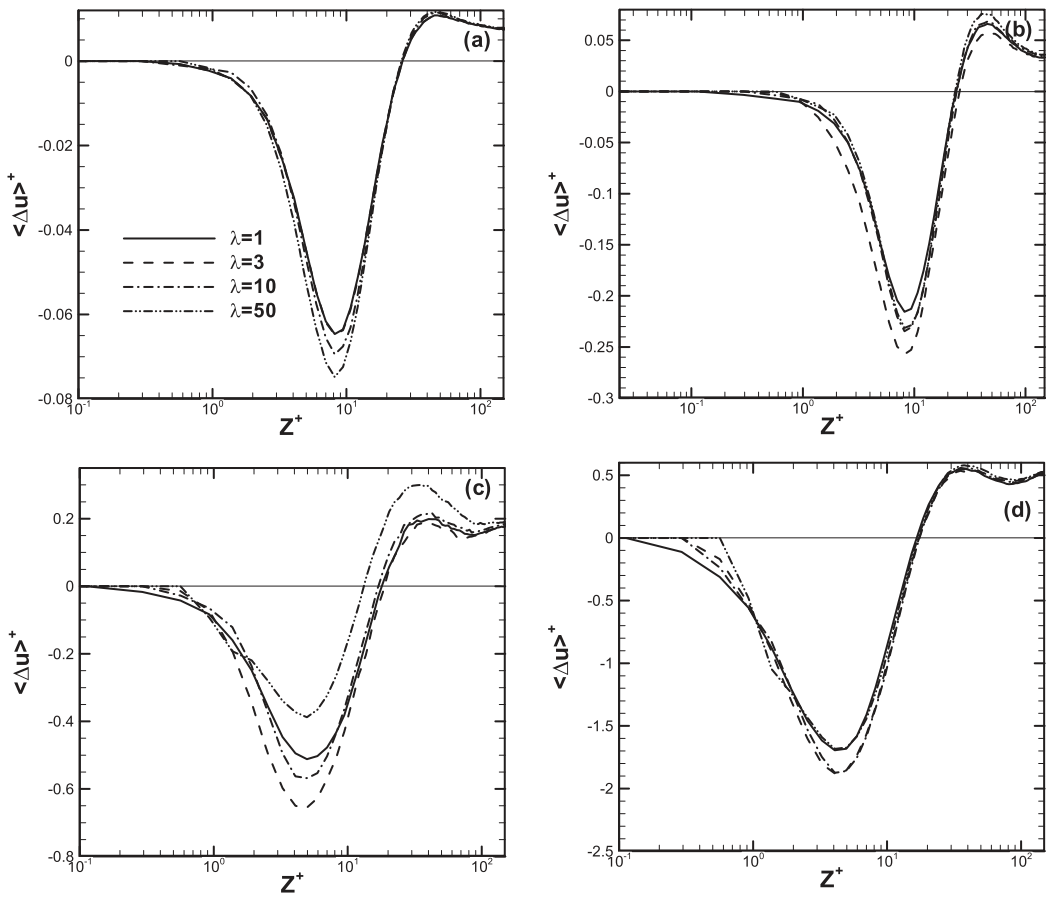

FIG. 14. Effect of fiber inertia and elongation on the mean streamwise slip velocity, $\langle \Delta u \rangle^+$. Panels: (a) $St = 1$; (b) $St = 5$; (c) $St = 30$; and (d) $St = 100$. Lines: ——— $\lambda = 1$, − − − $\lambda = 3$, − · − · − $\lambda = 10$, − · · − · · − $\lambda = 50$.

from the fluid over about 80% of the channel cross-section. The effect of fiber aspect ratio appears to be rather modest, as already suggested by the scatter plots in Figure 11. The most elongated fibers with $\lambda = 50$ behave somewhat different than the other fibers. The negative correlation between Δu^+ and u_p^+ is reduced next to the wall, whereas a stronger correlation is observed over the rest of the channel. The corresponding correlation between wall-normal slip velocity Δw^+ and wall-normal particle velocity w_p^+ in Figure 13(b) exhibits a qualitatively different behavior besides the negative peak in the vicinity of the wall at $z^+ \approx 10$. This correlation changes sign at $z^+ \approx 20$ and reaches a positive peak at about $z^+ \approx 40$. Another zero-crossing occurs in between $z^+ = 70$ and 80, beyond which the correlation again switches sign and the work done by the fluid on the fibers is again negative as it is next to the wall. Outside of the zero-crossing at $z^+ \approx 20$, a monotonic reduction of $\langle \Delta w \cdot w_p \rangle^+$ is observed with increasing fiber aspect ratio. The work contributed by wall-normal motions is only of the order of 1% of the more essential contribution from the streamwise direction in Figure 13(a). This explains why we focused on streamwise-associated events in the scatter plots of Figures 9–12.

The streamwise and wall-normal mean slip velocity components, indicated as $\langle \Delta u \rangle^+$ and $\langle \Delta w \rangle^+$, are shown in Figs. 14 and 15, respectively. In these two figures, results for fibers with $St = 5$ and $\lambda = 3$ are in good qualitative and quantitative agreement with those reported by Zhao and van Wachem,[5] whereas results for $St = 30$ and $\lambda = 1$, 3, 10 compare well with those of Mortensen *et al.*,[20] which were obtained at slightly higher Re_τ. The spanwise component is not shown as it is equal to zero everywhere (no momentum transfer), indicating that the sampling time is sufficient.

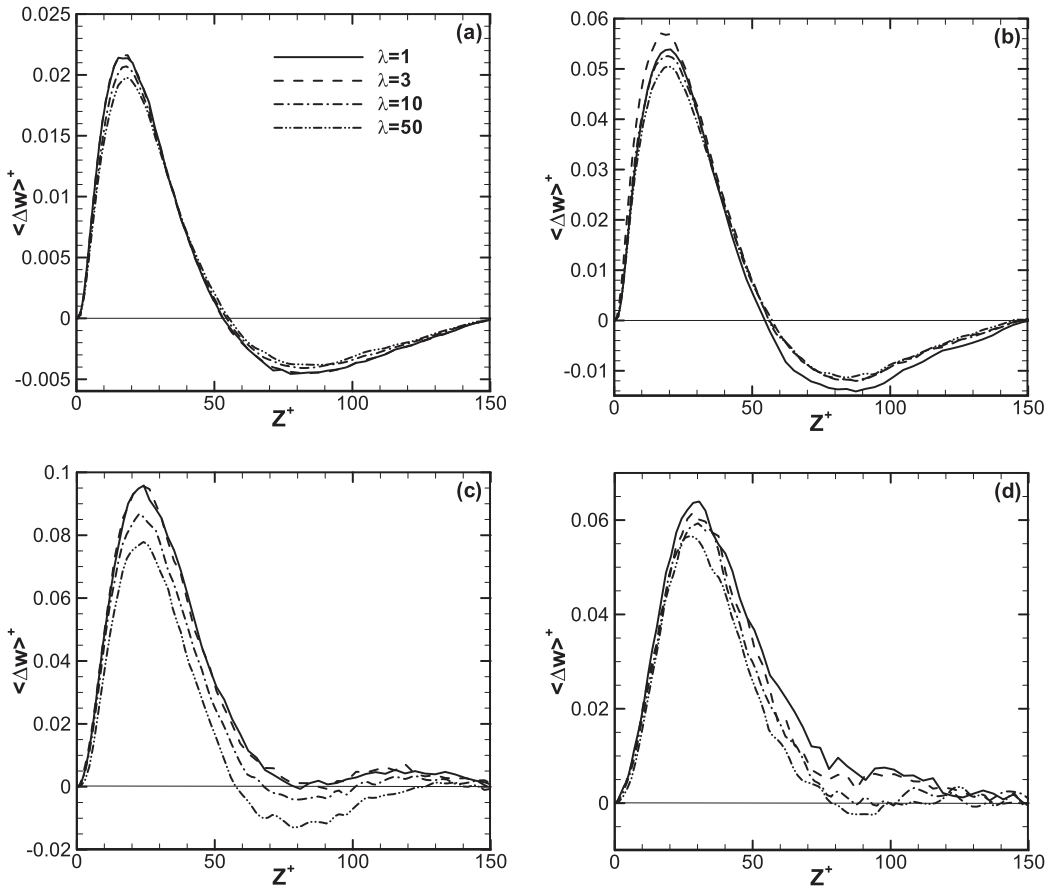

FIG. 15. Effect of fiber inertia and elongation on the mean wall-normal slip velocity, $\langle \Delta w \rangle^+$. Panels: (a) $St = 1$; (b) $St = 5$; (c) $St = 30$; and (d) $St = 100$. Lines as in Fig. 14.

The corresponding standard deviations (root-mean-square values), $rms(\Delta u')^+$ and $rms(\Delta w')^+$, are shown in Figs. 16 and 17, respectively.

First, we notice that the streamwise mean slip velocity $\langle \Delta u \rangle^+$ shows the same characteristic variation for all Stokes numbers. The negative values near the wall ($z^+ < 20$) indicate that the fibers (as well as the spherical particles[19]) lead the fluid whereas they lag behind the fluid throughout the central region, where $\langle \Delta u \rangle^+ > 0$. As noted by Zhao and van Wachem,[5] fibers obtain streamwise momentum from the fluid in the outer region of the flow ($z^+ > 20$, roughly) and add streamwise momentum to the fluid near the wall. In the present one-way coupled simulations, the fibers receive streamwise momentum from the fluid in the outer flow region and lose streamwise momentum in the vicinity of the walls. Only if the simulations had been two-way coupled, or in a physical laboratory experiment, the momentum received by the fibers in the core region would correspond to a loss of fluid momentum. Similarly, the fluid would gain streamwise momentum in the near-wall region only in two-way coupled simulations. This process appears to be driven mostly by inertia. Elongation determines a higher momentum exchange with the fluid, as indicated by the peak value attained by the slip velocity: this was observed also by Zhao and van Wachem,[5] who ascribed such behavior either to a higher mass loading of fibers or to fiber orientation or both. Since mass loading effects are disregarded in our study, it may be concluded that the amount of momentum transferred between the phases depends on how fibers orient themselves within the flow. It can be noticed that, for small St, λ-effects are limited to the region where $\langle \Delta u \rangle^+$ reaches the lowest negative value. For $St = 1$, these effects become appreciable only for $\lambda \geq 10$, whereas they are observed already at $\lambda = 3$ for the $St = 5$ fibers. In fact, these fibers exhibit a non-monotonic change of $\langle \Delta u \rangle^+$ with λ. The same trend is maintained by the $St = 30$ fibers, which however show a much lower near-wall velocity lead

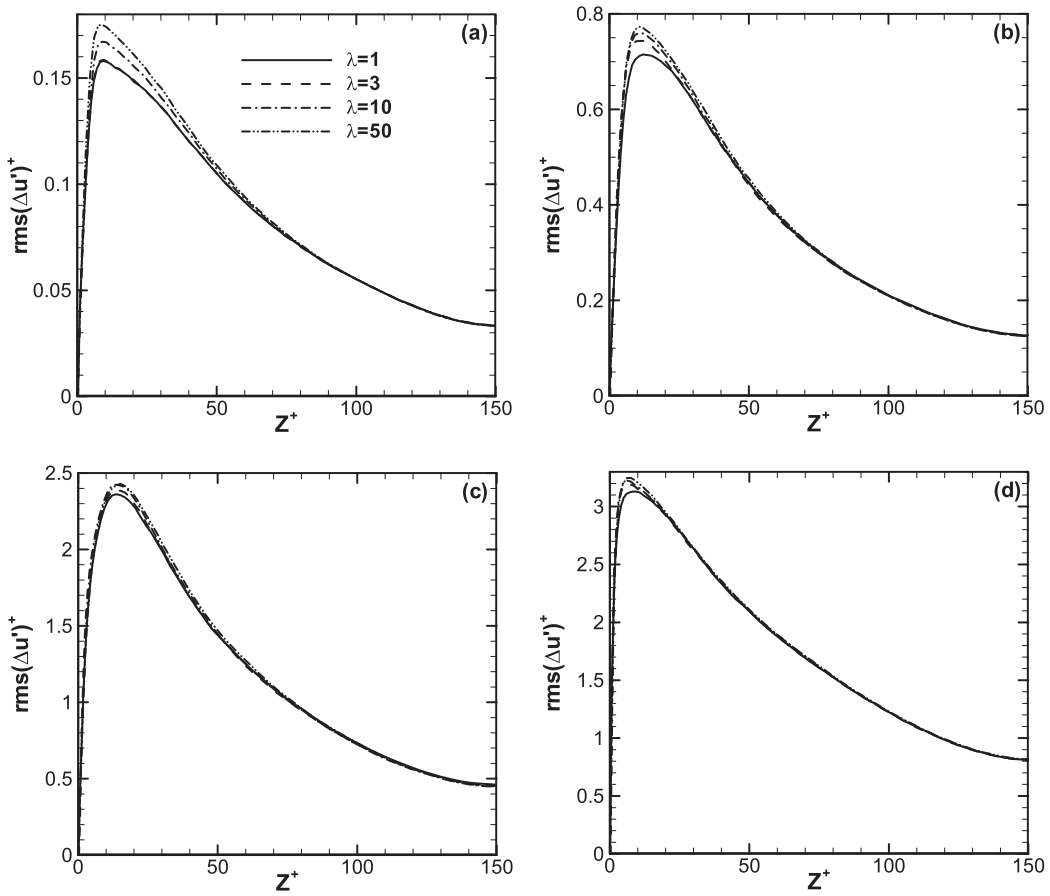

FIG. 16. Effect of fiber inertia and elongation on streamwise slip velocity rms, $rms(\Delta u')^+$. Panels: (a) $St = 1$; (b) $St = 5$; (c) $St = 30$; and (d) $St = 100$. Lines as in Fig. 14.

(and a much higher center-flow velocity lag) for $\lambda = 50$. For the $St = 100$ fibers, there is virtually no difference in the $\langle \Delta u \rangle^+$ profiles between spheres and longest ($\lambda = 50$) fibers and between the two intermediate fiber sets ($\lambda = 3$ and 10).

Similar considerations can be made for the wall-normal slip velocity $\langle \Delta w \rangle^+$, which provides a measure of how much of the momentum of the fibers is conveyed to the wall region. Fiber elongation mainly affects the positive near-wall peak, which becomes smaller in magnitude as λ increases. Stronger λ-induced modifications can be observed as fiber inertia increases: For $St = 30$ and $St = 100$ also the positive values of $\langle \Delta w \rangle^+$ undergo a quantitative change that is monotonic with elongation. These profiles indicate that fibers moving to the wall are dragging the fluid, while fibers leaving the wall move back with much lower momentum.[5] We remark that this process is observed also at steady state for fiber concentration.[5]

The observed behavior of the non-zero mean slip velocities has important implications not only for the momentum exchange between the continuous fluid phase and the discrete fiber phase, recently discussed by Zhao and van Wachem,[5] but also for the interphasial energy transfer, examined by Zhao *et al.*[51] for spherical particles in two-way coupled simulations. A major difference between the momentum exchange and the energy exchange is that the mechanical energy transferred from one phase to the other differs from the amount transferred the other way. According to Zhao *et al.*,[51] this difference can be interpreted as a particle-induced energy dissipation, which is proportional to $\langle \Delta \mathbf{u} \rangle^2$ and represents a loss of mechanical energy from the suspension.

Finally, we examine the streamwise and wall-normal components of the root mean square (rms) of the slip velocity. As already discussed in Ref. 19, rms values typically exceed the corresponding

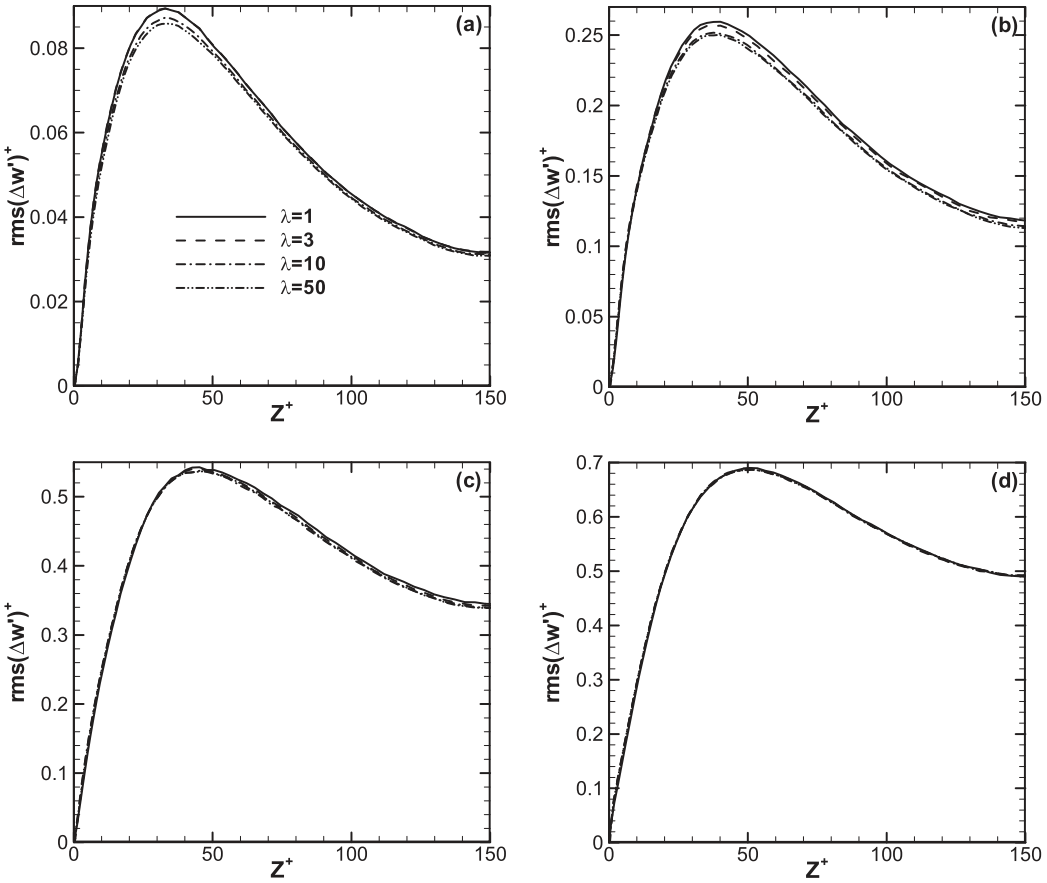

FIG. 17. Effect of fiber inertia and elongation on wall-normal slip velocity rms, $rms(\Delta w')^+$. Panels: (a) $St = 1$; (b) $St = 5$; (c) $St = 30$; and (d) $St = 100$. Lines as in Fig. 14.

mean value by roughly 3 to 5 times, revealing that the instantaneous slip velocity and, in turn, the drag force may easily change sign. More so for the longer fibers in the near-wall region, which exhibit higher streamwise fluctuations, as seen in Figs. 16(a) and 16(b). Elongation effects on rms values in the streamwise direction become less evident as fiber inertia increases, as shown in Figs. 16(c) and 16(d). Also, elongation plays a marginal role in modulating the wall-normal slip-velocity fluctuations, even at small St (see Fig. 17(a), for instance).

D. Reynolds number effects

In this section, we discuss the modifications on the slip velocity induced by an increase in the flow Reynolds number. In Fig. 18, we show the Re_τ-dependence of the mean and rms components of the streamwise and wall-normal slip velocity for the $St = 30$ fibers with $\lambda = 10$. The inset in Figs. 18(b)–18(d) shows the same quantities as a function of the wall distance in outer units, z/h. Overall, an increase of turbulence intensity leads to an increase of the magnitude of $\Delta\mathbf{u}^+$ near the wall. This increase is particularly evident for the mean velocities (Figs. 18(a) and 18(b)) and for the wall-normal rms (Fig. 18(d)). This means that the intermittency associated with the relative motion of fibers with respect to the surrounding fluid increases with Re_τ and hence may become more difficult to model. The opposite effect is observed outside the buffer layer, where profiles show a general decrease of mean and rms (evident when the wall-normal coordinate is scaled in outer units).

As expected, differences are generally small between the simulations at $Re_\tau = 150$ and $Re_\tau = 180$, but become more evident for $Re_\tau = 300$. It would be interesting to simulate values of Re_τ at least one order of magnitude higher than those considered here to evaluate fiber scaling behavior.

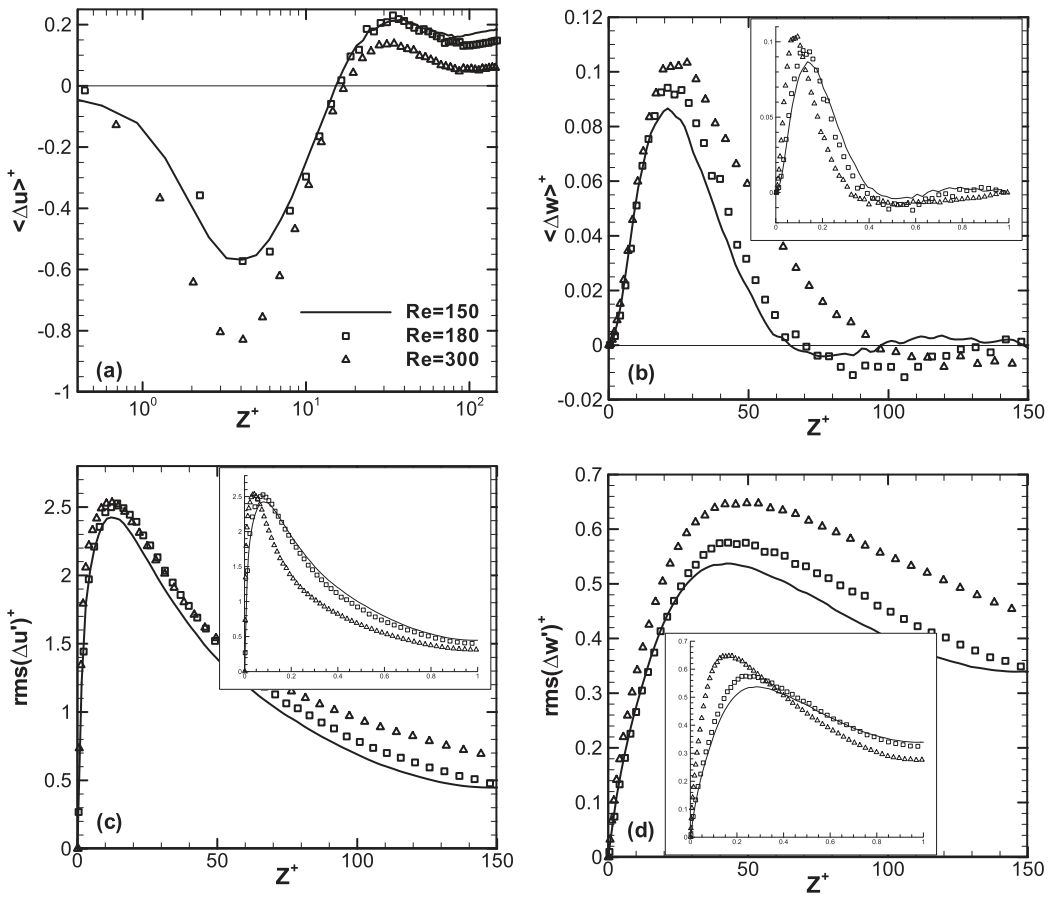

FIG. 18. Effect of Reynolds number on slip velocity statistics (for the reference case of fibers with $St = 30$ and $\lambda = 10$). Panels: (a) Mean streamwise slip velocity, $\langle \Delta u \rangle^+$; (b) mean wall-normal slip velocity, $\langle \Delta w \rangle^+$; (c) streamwise slip velocity fluctuation, $rms(\Delta u')^+$; and (d) wall-normal slip velocity fluctuation, $rms(\Delta w')^+$. Lines and symbols: ——— $Re_\tau = 150$, □ $Re_\tau = 180$, △ $Re_\tau = 300$. Insets in panels (b), (c), and (d) show mean and rms slip velocities as a function of the wall distance in outer units, z/h.

However, this analysis would require computationally expensive simulations (even for nowadays computers) and is beyond the scope of the present investigation.

V. CONCLUDING REMARKS

In this paper, the relative translational motion between fiber-like prolate ellipsoids suspended in turbulent channel flow and the surrounding fluid is examined using DNS (up to $Re_\tau = 300$) coupled with the Lagrangian tracking of point-wise fibers. The analysis is focused on the influence that fiber elongation (parameterized by the aspect ratio λ) has on the fiber-to-fluid slip velocity at varying fiber inertia (parameterized by the Stokes number St). The effect of the turbulence intensity (parameterized by the shear Reynolds number Re_τ) is also addressed.

Results show that elongation has a quantitative effect on slip velocity statistics, particularly evident for fibers with small St: elongation influences the peak value attained by the mean and rms slip velocities but not their qualitative wall-normal behavior. As St increases, differences due to the aspect ratio tend to vanish and the relative motion between individual fibers and the surrounding fluid is controlled by fiber inertia. Fibers approach the wall with a larger momentum than they have returning to the center of the channel. This is believed to cause the well-known concentration build-up occurring near the wall.[5] Once in the vicinity of the wall, fibers form long rows in regions of lower-than-mean fluid streamwise velocity fluctuations, where they are dragged forward by the

faster-moving fluid. The distribution of slip velocity values for fibers interacting with near-wall turbulent coherent structures (low/high speed streaks, sweeps and ejections) has been characterized by means of conditional statistics (PDFs and scatter plots). Such statistics highlight the correlation between fiber motion and local fluid structures, which ultimately determine the observed velocity differences between the phases. Our results indicate that the conditional PDFs (evaluated considering only fibers trapped either in sweeps or ejections or high/low-speed streaks) are in general non-Gaussian and therefore suggest that the relative motion of fibers with respect to the surrounding fluid cannot be modelled as a diffusion process with constant diffusion coefficient (namely, an Ornstein-Uhlenbeck process).[44] This does not exclude the possibility of modelling fiber-to-fluid rotation as a Lagrangian Stochastic diffusion process. In fact, such a process can yield Eulerian-conditioned PDFs that deviate from Gaussianity, provided a suitable non-constant diffusion term.[45,46,52,53] In this case, the Gaussian hypothesis is valid for conditional statistics of the increment of the variable being modelled over short time intervals, and applies when the process is conditioned on the initial value of such variable of the beginning of the time interval[45,46,52,53] (a situation quite different from that used in the present study).

The slip velocity appears to be modestly affected by the level of turbulence intensity, at least within the range of Reynolds numbers considered in the present study: No significant Reynolds number effects are observed, indicating that fiber dynamics exhibit a scaling behavior with respect to the shear velocity up to $Re_\tau = 300$.

Post-processed statistics and raw data for fiber position and velocity, extracted from the DNS repository examined in this work, are made freely available to interested users at http://www.fp1005.cism.it.

The point-particle formulation, as adopted in the present study, is a viable approach to simulate dilute fiber suspension flows. The formulation is, however, based on a number of simplifying assumptions. In order to make the formulation more physically grounded, we believe that the wall-collision modeling should be improved first. The recent paper by Ozolins and Strautins[54] may serve as a guide. An improved wall-collision model might be valuable irrespective of the fiber aspect ratio. Development of finite-Reynolds-number corrections for the force, as expressed in Eq. (4), and torque, as expressed in Eq. (6), acting from the viscous fluid on ellipsoidal particles will make the Lagrangian particle modeling more versatile. It may also be worthwhile to take the variation of the fluid velocity gradients into account, but this will only have a potential impact on the dynamics of the longest fibers. If one should aim to simulate fiber suspensions with a fairly high fiber concentration, fiber-fiber collisions will become important. A collision model for ellipsoidal-shaped particles was recently proposed by Zhao and van Wachem,[5] but interparticle collisions had only a negligible effect on the results of their simulations.

As a future development of this work, it would be interesting to characterize statistically the relative rotational motion between fibers and fluid in the (Re_τ, St, λ) parameter space. To this aim, we are currently performing new simulations to examine the slip spin produced by the difference between the angular velocity of the fiber and the angular velocity of the surrounding fluid. The slip spin is the primary variable in the quantification of the torque exerted by the fluid on the fibers, and is expected to exhibit stronger dependency on elongation than the slip velocity.

ACKNOWLEDGMENTS

Computing time was granted by CINECA Supercomputing Center (Bologna, Italy) and by the Research Council of Norway (Programme for Supercomputing). L.Z. has been funded by The Research Council of Norway through project no. 213917/F20 "Turbulent Particle Suspensions." Funding of a Short Term Scientific Mission (STSM) by COST Action FP1005 "Fiber suspension flow modelling: a key for innovation and competitiveness in the pulp and paper industry" is greatly appreciated. The authors also thank Professor Alfredo Soldati for providing the pseudo spectral code[28] that were used in this study and the Referees for their useful remarks and comments. H.I.A. appreciates the hospitality of The International Centre for Mechanical Sciences (CISM) in Udine.

[1] F. Lundell, L. D. Söderberg, and P. H. Alfredsson, "Fluid mechanics of papermaking," Annu. Rev. Fluid Mech. **43**, 195–217 (2011).
[2] A. B. Metzner, "Rheology of suspensions in polymeric liquids," J. Rheol. **29**, 739–775 (1985).
[3] L. Sabban and R. van Hout, "Measurements of pollen grain dispersal in still air and stationary, near homogeneous, isotropic turbulence," J. Aerosol. Sci. **42**, 867–882 (2011).
[4] R. C. Moffet and K. A. Prather, "In-situ measurements of the mixing state and optical properties of soot with implications for radiative forcing estimates," Proc. Natl. Acad. Sci. U.S.A. **106**, 11872–11877 (2009).
[5] F. Zhao and B. G. M. van Wachem, "Direct numerical simulation of ellipsoidal particles in turbulent channel flow," Acta Mech. **224**, 2331–2358 (2013).
[6] H. I. Andersson and A. Soldati, "Anisotropic particles in turbulence: Status and outlook," Acta Mech. **224**, 2219–2224 (2013).
[7] L. H. Zhao, H. I. Andersson, and J. J. J. Gillissen, "Turbulence modulation and drag reduction by spherical particles," Phys. Fluids **22**, 081702 (2010).
[8] Z. Shang, J. Lou, and H. Li, "A novel Lagrangian algebraic slip mixture model for two-phase flow in horizontal pipe," Chem. Eng. Sci. **102**, 315–323 (2013).
[9] M. Šimčik, A. Mota, M. C. Ruzicka, A. Vicente, and J. Texeira, "CFD simulation and experimental measurement of gas holdup and liquid interstitial velocity in internal loop airlift reactor," Chem. Eng. Sci. **66**, 3268–3279 (2011).
[10] K. A. Pericleous and S. N. Drake, "An algebraic slip model of PHEONICS for multi-phase applications," in *Numerical Simulation of Fluid Flow and Heat/Mass Transfer Processes*, Lecture Notes in Engineering Vol. 18, edited by N. C. Markatos, M. Cross, D. G. Tatchell, and N. Rhodes, (Springer-Verlag, Berlin/Heidelberg, 1986) , pp. 375–385.
[11] C. Marchioli, M. V. Salvetti, and A. Soldati, "Appraisal of energy recovering sub-grid scale models for large-eddy simulation of turbulent dispersed flows," Acta Mech. **201**, 277–296 (2008).
[12] F. Bianco, S. Chibbaro, C. Marchioli, M. V. Salvetti, and A. Soldati, "Intrinsic filtering errors of Lagrangian particle tracking in LES flow fields," Phys. Fluids **24**, 045103 (2012).
[13] M. I. Yudine, "Physical considerations on heavy-particle diffusion," Adv. Geophys. **6**, 185—191 (1959).
[14] G. T. Csanady, "Turbulent diffusion of heavy particles in the atmosphere," J. Atmos. Sci. **20**, 201–208 (1963).
[15] M. R. Wells and D. E. Stock, "The effects of crossing trajectories on the dispersion of particles in a turbulent flow," J. Fluid Mech. **136**, 31–62 (1983).
[16] O. Simonin, E. Deutsch, and J. P. Minier, "Eulerian prediction of fluid particle correlated motion in turbulent two-phase flows," Appl. Sci. Res. **51**, 275–283 (1993).
[17] J. P. Minier and E. Peirano, "The pdf approach to turbulent polydispersed two-phase flows," Phys. Rep. **352**, 1–214 (2001).
[18] B. Oesterlé, "On heavy particle dispersion in turbulent shear flows: 3-D analysis of the effects of crossing trajectories," Boundary-Layer Meteorol. **130**, 71–95 (2009).
[19] L. H. Zhao, C. Marchioli, and H. I. Andersson, "Stokes number effects on particle slip velocity in wall-bounded turbulence and implications for dispersion models," Phys. Fluids **24**, 021705 (2012).
[20] P. H. Mortensen, H. I. Andersson, J. J. J. Gillissen, and B. J. Boersma, "Dynamics of prolate ellipsoidal particles in a turbulent channel flow," Phys. Fluids **20**, 093302 (2008).
[21] H. Zhang, G. Ahmadi, F. G. Fan, and J. B. McLaughlin, "Ellipsoidal particles transport and deposition in turbulent channel flows," Int. J. Multiphase Flow **27**, 971–1009 (2001).
[22] C. Marchioli, M. Fantoni, and A. Soldati, "Orientation, distribution, and deposition of elongated, inertial fibers in turbulent channel flow," Phys. Fluids **22**, 033301 (2010).
[23] I. Gallily and A. H. Cohen, "On the orderly nature of the motion of nonspherical aerosol particles. II. Inertial collision between a spherical large droplet and axially symmetrical elongated particle," J. Colloid Interface Sci. **68**, 338–356 (1979).
[24] H. Brenner, "The Stokes resistance of an arbitrary particle IV: Arbitrary fields of flow," Chem. Eng. Sci. **19**, 703–727 (1964).
[25] L. Schiller and A. Z. Naumann, "Über die grundlegenden Berechnungen bei der Schwerkraftaufbereitung," Z. Ver. Deutsch. Ing. **77**, 318 (1933).
[26] G. B. Jeffery, "The motion of ellipsoidal particles immersed in a viscous fluid," Proc. R. Soc. **102**, 161–179 (1922).
[27] M. Shapiro and M. Goldenberg, "Deposition of glass fiber particles from turbulent air flow in a pipe," J. Aerosol. Sci. **24**, 65–87 (1993).
[28] A. Soldati and C. Marchioli, "Physics and modelling of turbulent particle deposition and entrainment: Review of a systematic study," Int. J. Multiphase Flow **35**, 827–839 (2009).
[29] C. Marchioli, A. Soldati, J. G. M. Kuerten, B. Arcen, A. Tanière, G. Goldensoph, K. D. Squires, M. F. Cargnelutti, and L. M. Portela, "Statistics of particle dispersion in direct numerical simulations of wall-bounded turbulence: Results of an international collaborative benchmark test," Int. J. Multiphase Flow **34**, 879–893 (2008).
[30] J. K. Eaton, "Two-way coupled turbulent simulations of gas-particle flows using point-particle tracking," Int. J. Multiphase Flow **35**, 792–800 (2009).
[31] S. Balachandar and J. K. Eaton, "Turbulent dispersed multiphase flow," Annu. Rev. Fluid Mech. **42**, 111–133 (2010).
[32] S. Elghobashi, "On predicting particle-laden turbulent flows," Appl. Sci. Res. **52**, 309–329 (1994).
[33] J. Kim, P. Moin, and R. Moser, "Turbulence statistics in fully developed channel flow at low Reynolds number," J. Fluid Mech. **177**, 133–166 (1987).
[34] C. Marchioli and A. Soldati, "Mechanisms for particle transfer and segregation in turbulent boundary layer," J. Fluid Mech. **468**, 283–315 (2002).
[35] D. W. I. Rouson and J. K. Eaton, "On the preferential concentration of solid particles in turbulent channel flow," J. Fluid Mech. **428**, 149–169 (2001).
[36] J. R. Fessler, J. D. Kulick, and J. K. Eaton, "Preferential concentration of heavy particles in a turbulent channel flow," Phys. Fluids **6**, 3742–3749 (1994).
[37] A. W. Vreman, "Turbulence characteristics of particle-laden pipe flow," J. Fluid Mech. **584**, 235–279 (2007).

[38] J. D. Kulick, J. R. Fessler, and J. K. Eaton "Particle response and turbulence modification in fully developed channel flow," J. Fluid Mech. **277**, 109–134 (1994).
[39] C. D. Dritselis and N. S. Vlachos, "Numerical invesigation of momentum exchange between particles and coherent structures in low Re turbulent channel flow," Phys. Fluids **23**, 025103 (2011).
[40] M. Righetti and G. P. Romano, "Particle-fluid interactions in a plane near-wall turbulent flow," J. Fluid Mech. **505**, 93–121 (2004).
[41] A. Guha, "Transport and deposition of particles in turbulent and laminar flow," Annu. Rev. Fluid Mech. **40**, 311–341 (2008).
[42] K. M. O. Håkansson, M. Kvick, F. Lundell, L. P. Wittberg, and L. D. Söderberg, "Measurement of width and intensity of particle streaks in turbulent flows," Exp. Fluids **54**, 1555 (2013).
[43] W. Willmarth and S. Lu, "Structure of the Reynolds stress near the wall," J. Fluid Mech. **55**, 65–92 (1972).
[44] C. Marchioli and A. Soldati, "Rotation statistics of fibers in wall shear turbulence," Acta Mech. **224**, 2311–2330 (2013).
[45] P. Chibbaro and J.-P. Minier, *Stochastic Methods for Fluid Mechanics*, CISM, International Centre for Mechanical Sciences Vol. 548 (Springer-Verlag, Berlin, 2014).
[46] M. Guingo and J.-P. Minier, "A stochastic model of coherent structures for particle depostition in turbulent flows," Phys. Fluids **20**, 053303 (2008).
[47] M. Manhart, "Rheology of suspensions of rigid-rod like particles in turbulent channel flow," J. Non-Newtonian Fluid Mech. **112**, 269–293 (2003).
[48] L. H. Zhao, H. I. Andersson, and J. J. J. Gillissen, "On inertial effects of long fibers in wall turbulence: Fiber orientation and fiber stresses," Acta Mech. **224**, 2375–2384 (2013).
[49] B. T. Chao, "Turbulent transport behavior of small particles in dilute suspensions," Österr. Ing. Arch. **18**, 7–21 (1964).
[50] S. E. Elghobashi and T. W. Abou Arab, "A two-equation turbulence model for two-phase flows," Phys. Fluids **26**, 931–938 (1983).
[51] L. H. Zhao, H. I. Andersson, and J. J. J. Gillissen, "Interphasial energy transfer and particle dissipation in particle-laden wall turbulence," J. Fluid Mech. **715**, 32–59 (2013).
[52] S. B. Pope, "Lagrangian pdf methods for turbulent reactive flows," Annu. Rev. Fluid Mech. **26**, 23–63 (1994).
[53] S. B. Pope, *Turbulent Flow* (Cambridge University Press, 2000).
[54] A. Ozolins and U. Strautins, "Simple models for wall effect in fiber suspension flows," Math. Modell. Anal. **19**, 75–84 (2014).